

https://doi.org/10.1093/petrology/egac068
Original Manuscript

# P-T-t Path of Unusual Garnet-Kyanite-Staurolite-Amphibole Schists, Ellesmere Island, Canada—Quartz Inclusion in Garnet Barometry and Monazite Petrochronology

Karolina Kośmińska<sup>1,2,\*</sup>, Jane A. Gilotti<sup>1,2</sup>, William C. McClelland<sup>2</sup>, Matthew A. Coble<sup>3</sup> and Jay B. Thomas<sup>4</sup>

- <sup>1</sup>Faculty of Geology, Geophysics and Environmental Protection, AGH-University of Science and Technology, Kraków 30-059 Poland
- <sup>2</sup>Department of Earth and Environmental Sciences, University of Iowa, Iowa City, IA 52242 USA
- <sup>3</sup>Surface Geosciences Department, GNS Science, Lower Hutt, 5010, New Zealand
- <sup>4</sup>Department of Earth & Environmental Sciences, Syracuse University, Syracuse, NY 13244, USA
- \*Corresponding author. Present address: Faculty of Geology, Geophysics and Environmental Protection, AGH-University of Science and Technology, Kraków 30-059 Poland.
- Telephone: + 48 12 617 21 48. Fax: + 48 12 617 21 48. E-mail: karolina.kosminska@agh.edu.pl

#### **Abstract**

Garnet-kyanite-staurolite assemblages with large, late porphyroblasts of amphibole form garbenschists in Ordovician volcaniclastic rocks lying immediately south of the Pearya terrane on northernmost Ellesmere Island, Canada. The schist, which together with carbonate olistoliths makes up the Petersen Bay Assemblage (PBA), displays a series of parallel isograds that mark an increase in metamorphic grade over a distance of 10 km towards the contact with Pearya; however, a steep, brittle Cenozoic strike-slip fault with an unknown amount displacement disturbs the earlier accretionary relationship. The late amphibole growth, probably due to fluid ingress, is clear evidence of disequilibrium conditions in the garbenschist. In order to recover the P-T history of the schists, we construct isochemical phase equilibrium models for a nearby garnet-mica schist that escaped the fluid event and compare the results to quartz inclusion in garnet (QuiG) barometry for a garbenschist and the metapelitic garnet schist. Quartz inclusions are confined to garnet cores and the QuiG results, combined with Ti-in-biotite and garnet-biotite thermometry, delineate a prograde path from 480 to 600°C and 0.7 to 0.9 GPa. This path agrees with growth zoning in garnet deduced from X-ray maps of the spessartine component in garnet. The peak conditions obtained from pseudosection modelling using effective bulk composition and the intersection of garnet rim with matrix biotite and white mica isopleths in the metapelite are 665°C at ≤0.85 GPa. Three generations of monazite (I, II and III) were identified by textural characterization, geochemical composition (REE and Y concentrations) and U-Pb ages measured by ion microprobe. Monazite I occurs in the matrix and as inclusions in garnet rims and grew at peak P-T conditions at  $397 \pm 2$  Ma  $(2\sigma)$  from the breakdown of allanite. Monazite II forms overgrowths on matrix Monazite I grains that are oriented parallel to the main schistosity and yield ages of  $385 \pm 2$  Ma. Monazite III, found only in the garbenschist, is  $374 \pm 6$  Ma, which is interpreted as the time of amphibole growth during fluid infiltration at lower temperature and pressure on a clockwise P-T path that remained in the kyanite stability field. These results point to a relatively short (≈12 Myr) Barrovian metamorphic event that affected the schists of the PBA. An obvious heat source is lacking in the adjacent Pearya terrane, but we speculate it was large Devonian plutons—similar to the  $390 \pm 10$  Ma Cape Woods granite located 40 km across strike from the fault—that have been excised by strike-slip. Arc fragments that are correlative to the PBA are low grade; they never saw the heat and were not directly involved in Pearya accretion.

Keywords: U-Pb geochronology, QuiG, Pearya, P-T pseudosection, monazite, garbenschist

#### INTRODUCTION

The Petersen Bay Assemblage (PBA) on northern-most Ellesmere Island (Fig. 1) contains volcaniclastic schists with the unusual assemblage garnet + kyanite + staurolite + amphibole (Klaper & Ohta, 1993). The amphibole commonly forms late, feathery porphyroblasts up to 10 cm long that are characteristic of garbenschist. Similar schists have been described from the Tauern Window in the Austrian Alps (Selverstone et al., 1984), the Sierra de Pie de Palo, Argentina (Casquet et al., 2001;

Mulcahy et al., 2011) and adjacent to the Coast Mountains batholith in southeastern Alaska (McClelland et al., 1991). Subsets of this assemblage have also been reported from amphibolites with igneous origins (e.g. Helms et al., 1987; Kuyumjian, 1998; Tsujimori & Liou, 2004; Faryad & Hoinkes, 2006; Scott et al., 2009). Establishing the metamorphic evolution of garbenschist is challenging, in part because the unoriented amphibole neoblasts clearly grow late in the history and deciphering equilibrium assemblages can be difficult (Steffen & Selverstone,

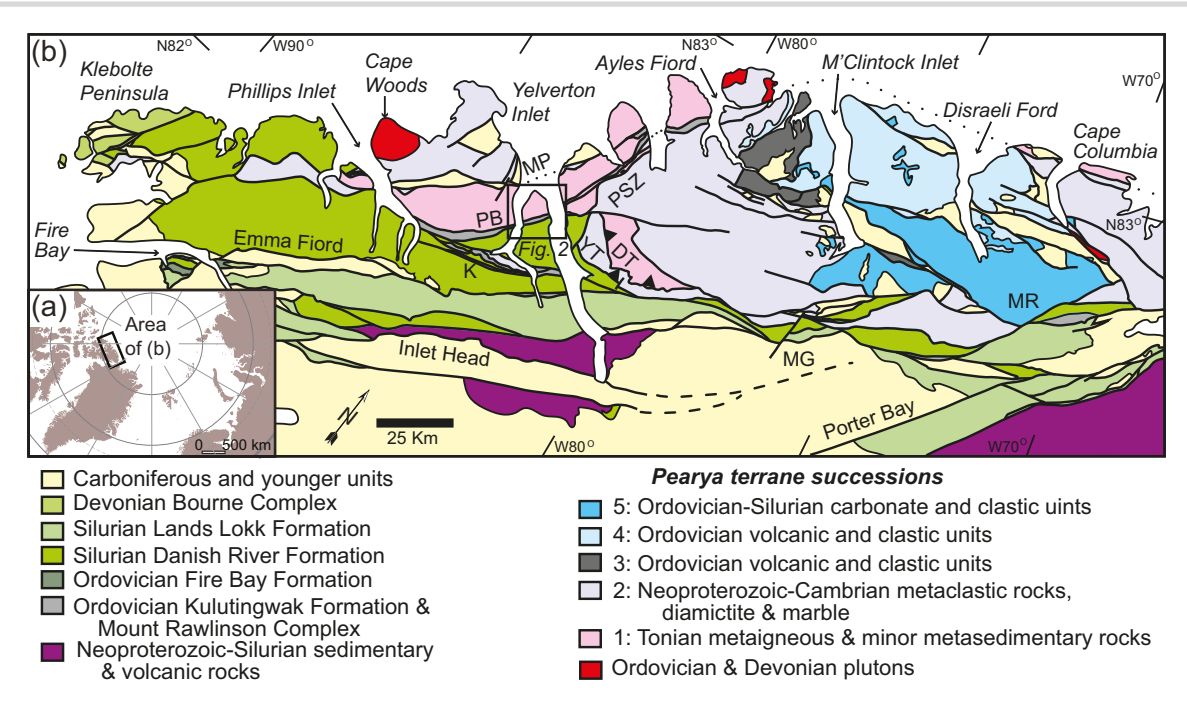


Fig. 1. (a) Polar projection of the Arctic region. (b) Simplified geologic map of northern Ellesmere Island after Trettin (1998). The following fault zones are abbreviated as: DT, Deuchars thrust; K, Kulutingwak fault; MG, M'Clintock Glacier fault; MP, Mitchell Point fault; MR, Mount Rawlinson fault; PB, Petersen Bay fault zone; PSZ, Pearya shear zone; YT, Yelverton thrust.

2006). With the obvious disequilibrium texture and growth of amphibole associated with late fluid influx, thermodynamic modeling to obtain metamorphic conditions is not applicable to the garbenschist (Lanari & Duesterhoeft, 2019). Fatehi et al. (2017) propose that hornblende in some garbenschist may even precipitate from hydrothermal fluids, which further complicates peak pressure (P) – temperature (T) estimates.

The PBA displays the highest grade of metamorphism seen along the entire accretionary contact with the composite, exotic Pearya terrane to the northwest. Steep, evenly spaced isograds in the volcaniclastic schists and adjacent turbidites require a local heat source in Pearya to cause the metamorphism (Fig. 2a). Despite truncation of the Tonian granitic gneiss of Pearya against the PBA due to late, Cenozoic brittle displacement, metamorphism in the PBA is the best target for understanding the timing and physical conditions of accretion. Speculation on the age of accretion ranges from Late Silurian from stratigraphic arguments (Trettin, 1987) to Early Carboniferous (Piepjohn et al., 2013; Piepjohn & von Gosen, 2018). The latter authors view the emplacement of the Pearya terrane as causing the sizeable fold-and-thrust belt of the Ellesmerian orogeny on the Laurentian margin. There are, however, no direct dates for this accretionary event.

The low variance volcaniclastic schists of the PBA are good candidates for geothermobarometry. Pressure is an important variable in the formation of the unusual garbenschist assemblage (Arnold et al., 2000), with typical estimates ranging from Barrovian conditions at ≈1 GPa (Selverstone et al., 1984) to near eclogite facies (up to 1.9 GPa; Tsujimori & Liou, 2004). Determining P is fraught with difficulty, especially when applying conventional

thermobarometry, which requires choosing the correct, equilibrium mineral compositions to match the proposed metamorphic evolution. Quartz-in-garnet (QuiG) elastic thermobarometry provides a relatively simple way to estimate pressure independent of mineral equilibrium (Angel et al., 2014; Kohn, 2014; Spear et al., 2014; Thomas & Spear, 2018; Gonzalez et al., 2019; Alvaro et al., 2020) and is widely applicable because quartz inclusions are very common in garnet porphyroblasts. The QuiG technique is especially practical for situations with complex metamorphic growth histories that can be gleaned from garnet zoning (e.g. Kośmińska et al., 2020; Wolfe & Spear, 2020; Wolfe et al., 2021). QuiG is also useful in evaluating P-T estimates derived from compositional zoning in terms of equilibrium versus metastable reaction overstepping (Castro & Spear, 2017; Spear & Wolfe, 2020).

Establishing the timing of metamorphism requires dating radiometric accessory minerals that can be linked to the P-T path in a process referred to as petrochronology (Engi et al., 2017). Monazite is a common accessory mineral in a variety of metamorphic rocks including medium P schists (e.g. Spear, 2010; Engi, 2017) and one of the main hosts of U and Th. Different generations of monazite can be recognized based on textural and compositional characteristics (Kohn et al., 2005; Dumond et al., 2015); they can record multiple events and a complex history. In-situ monazite dating allows for preservation of textural context while targeting different growth zones (Catlos et al., 2002; Williams & Jercinovic, 2012; Kylander-Clark et al., 2013; Hallett & Spear, 2015). Thus, monazite has proven to be a useful mineral for constraining time (t) on the P-T path of complex metamorphic rocks (e.g. Štípská et al., 2015; Engi, 2017).

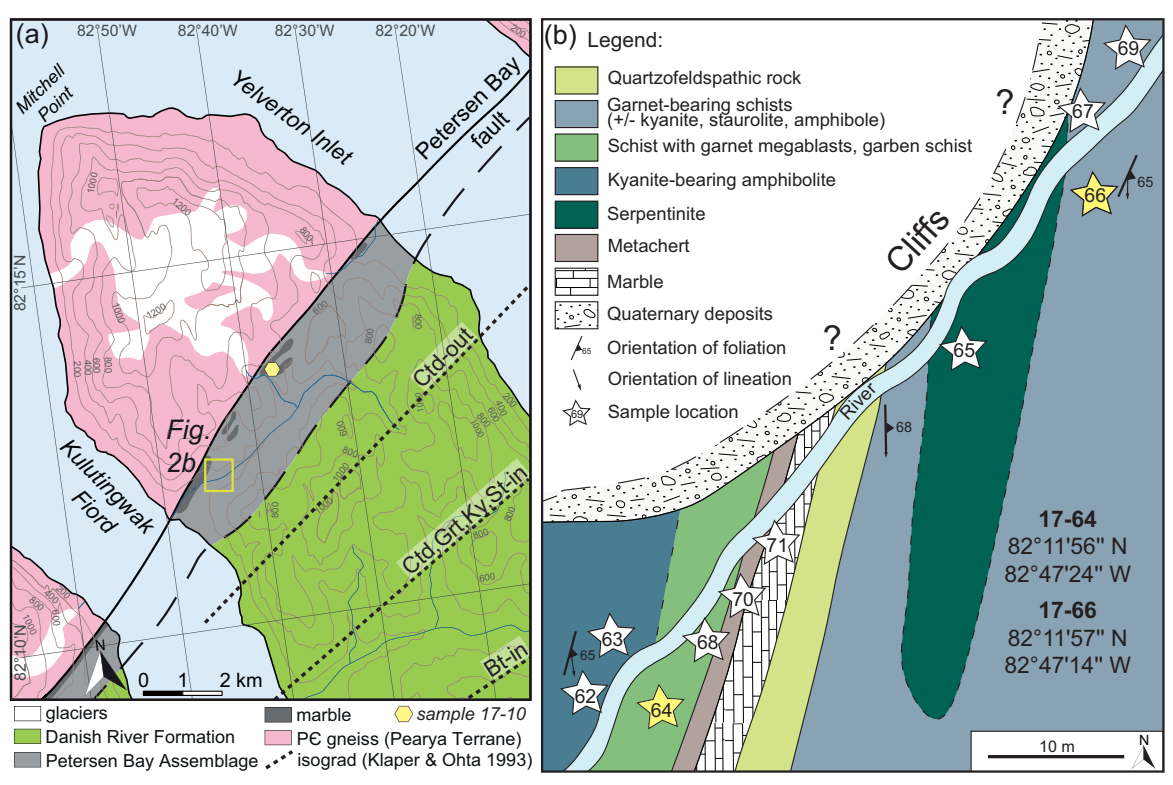


Fig. 2. (a) Geological map of the Mitchell Point peninsula modified from Trettin & Frisch (1996); metamorphic isograds are from Klaper & Ohta (1993). (b) Detailed geological map of the studied outcrop showing small-scale variation in lithology. Stars indicate sample locations. Yellow stars are samples chosen for petrochronological studies.

Textural relationships and trace element patterns help link the growth of monazite to the formation of other major and accessory minerals such as garnet (Foster et al., 2000; Pyle & Spear, 2003; Kohn et al., 2005; Rubatto et al., 2013; Dumond et al., 2015; Mottram et al., 2014; Petrík et al., 2019).

This study focuses on two monazite-bearing samples to establish a P-T-t path for the unit that includes the unusual garbenschists of the PBA. Phase equilibrium thermodynamic modeling of a garnet-bearing and amphibole-absent metapelite is used to establish a partial P-T path because the garnet-kyanite-staurolite garbenschist, with its post-tectonic, fluid-facilitated overgrowths of large amphibole, is not suitable for modeling. We apply the QuiG technique to both the metapelite and the garbenschist to further establish the P of garnet growth during a Barrovian metamorphic event. Monazite with three different textures and compositions can be tied to the petrology and is dated with insitu secondary ion mass spectrometry techniques. The timing of the peak Barrovian metamorphism most likely reflects the accretion of the Pearya terrane simultaneous with subduction-related(?) magmatism in the Middle Devonian.

#### **GEOLOGICAL SETTING**

The composite Pearya Terrane (Trettin, 1987, 1998) constitutes northernmost Ellesmere Island in the Canadian Arctic archipelago (Fig. 1). Pearya is an amalgamation of a Tonian crystalline arc, a low-grade package of Neoproterozoic to Paleozoic metasedimentary rocks, an Ordovician sub-arc igneous complex and volcaniclastic units that are unconformably overlain by middle Ordovician to Silurian sedimentary rocks (Trettin, 1998; Malone et al., 2014, 2017, 2019; Estrada et al., 2018). Pearya is the only exotic element recognized along the Arctic margin of Laurentia, and its accretionary history is enigmatic (McClelland et al., 2022). The Pearva terrane is separated from the Laurentian margin deep-water deposits and platform sedimentary rocks of the Neoproterozoic to early Paleozoic Franklinian basin (Dewing et al., 2019 and references therein) by a belt of rocks dominated by Silurian flysch, but also containing puzzling Ordovician-Silurian volcanic rocks and metamorphic rocks of uncertain age and affinity (Trettin, 1998). The flysch, known as the Danish River and Lands Lokk formations (Trettin, 1998), comprises turbiditic deposits that blanket the underlying Franklinian basin. Isolated sedimentary and volcanic sections with possible arc affinities, such as the Ordovician Kulutingwak formation (Bjørnerud & Bradley, 1992; Trettin, 1998) and the Fire Bay volcanic assemblage (Koch et al., 2022), lie adjacent to prominent strike-slip faults (Fig. 1b). The sedimentary rocks of the Franklinian basin, Kulutingwak formation and flysch are folded together above a proposed decollément lying above Paleoproterzoic Laurentian basement (Piepjohn & von Gosen, 2018).

The steep Petersen Bay fault zone marks the southern boundary of Pearya west of Yelverton Inlet (Fig. 1b). The older, ductile shear zone has been interpreted as either a SE-directed overturned thrust (Klaper, 1992) or a significant translational zone formed in transpression (Trettin, 1987; McClelland et al., 2021, 2022). The current Petersen Bay fault is a Cenozoic, brittle structure with both dextral and sinistral strike-slip shear sense (Piepjohn et al., 2013; Piepjohn & von Gosen, 2018). Cataclasites, locally up to a few hundred meters thick, suggest substantial brittle translation, although the amount of Cenozoic displacement is unknown (McClelland et al., 2022). Northwest of the fault, the Pearya terrane is characterized by mediumgrade, polydeformed, Tonian orthogneiss and associated paragneiss (Trettin, 1998; Malone et al., 2017; Estrada et al., 2018). The unusual schists of this study (Fig. 2) are part of the PBA (Klaper, 1992), which forms a 22 km long and 1–3 km wide layer lying immediately southeast of the fault zone (Trettin & Frisch, 1996). The PBA is assumed to be in depositional contact with the younger Danish River formation to the southeast (Klaper, 1992).

The PBA consists of marble, amphibole ± garnet schist, amphibolite, serpentinite and minor psammitic and pelitic schists. The PBA has been correlated with the lower-grade Ordovician Kulutingwak Formation (Trettin & Frisch, 1996; Trettin, 1998), which has been interpreted as a carbonate-volcanic association with arc affinity (Bjørnerud, 1991; Bjørnerud & Bradley, 1992). We retain the original name here (i.e. PBA) to distinguish the higher-grade metamorphic rocks of the study area from lower grade sections along other faults. The rocks of the PBA have a steep schistosity that is approximately parallel to the strike of the Petersen Bay fault; stretching lineations are uncommon in the schists (Klaper, 1992). Klaper & Ohta (1993) estimated peak metamorphic conditions up to 600°C and 0.6 GPa for garnet-kyanite schist from the PBA. They also defined a series of isograds extending southeastward over a distance of 10 km from amphibolite to greenschist facies (Fig. 2a). The age of metamorphism has not been directly determined; however,  $^{40}$ Ar/ $^{39}$ Ar plateau ages of 433 ± 3 Ma on hornblende from a PBA schist and 322 ± 2 Ma from muscovite in a cross-cutting pegmatite (Trettin et al., 1992) put some limits on the timing.

Our study focuses on an outcrop of exceptionally wellpreserved PBA lithologies located in a stream that was accessible during low meltwater conditions (Fig. 2b). In contrast, much of the PBA along the fault zone (Fig. 2a) is considerably altered by pervasive, late CO2-rich fluids. The studied locality is a mixture of at least seven lithologies suggestive of a deformed mélange in an arc environment (Figs 2b and 3; Table 1). Massive amphibolite with visible kyanite but no garnet occurs in the SE part of the outcrop (samples 17-62, 17-63; Fig. 3a, b) and serpentinite forms prominent lenses (sample 17-65, Fig. 3c). Quartzofeldspathic psammite, metachert and marble constitute a package of cm-thick layers (samples 17-71, 17-70; Fig. 3d). A variety of garnet-bearing schists (samples 17-66, 17-67 and 17-69, Fig. 3f-h), locally with garnet megablasts up to 5 cm (sample 17-68, Fig. 3e), are

common. In some places, the schistosity is overprinted by amphibole sheaves forming garbenschist (sample 17-64, Fig. 3f); these are typically the rocks with the lowest variance assemblage. Two samples, metapelite 17-66 and garbenschist 17-64, contain monazite and were thus suitable for petrochronological analysis.

#### **METHODS**

## Mineral and whole rock chemistry

The mineral chemistry and X-ray concentration maps were determined by wavelength dispersive spectrometry using a JEOL JXA-8230 Superprobe Electron Probe Microanalyser (EPMA) at the University of Iowa, Iowa City, IA. The operating conditions for the spot analyses were 20 nA beam current, 15 kV accelerating voltage and counting times of 10 s on peaks and 5 s on background. The beam size varies from 1  $\mu$ m to 10  $\mu$ m depending on the mineral. Natural mineral standards were used for calibration. Representative analyses are reported in Tables 2-4. Garnet X-ray mapping of major and trace element composition was performed with 15 kV accelerating voltage, 100 nA beam current and 100 ms dwell time. Mapping of monazite used a similar routine, with a shorter dwell time of 50 ms. The pixel size for X-ray maps varied depending on the size of the individual grains or porphyroblasts. X-ray maps were processed using the software ImageJ (Schneider et al., 2012). Mineral abbreviations are after Whitney & Evans (2010).

The bulk rock composition of five samples was determined by X-ray fluorescence at the Bureau Veritas Mineral Laboratories in Canada (Table S1). Samples were fused with LiBO<sub>2</sub>/Li<sub>2</sub>B<sub>4</sub>O<sub>7</sub>.

## Phase equilibrium modelling

Isochemical phase equilibrium modelling to produce P-T pseudosections was performed using Perple\_X software version 6.8.4 (Connolly, 1990, 2005) with the internally consistent thermodynamic database by Holland & Powell (2011) in the MnO-Na<sub>2</sub>O-K<sub>2</sub>O-CaO-FeO-MgO- $Al_2O_3-SiO_2-H_2O-TiO_2-O_2$  (MnNKCFMASHTO) system. The amount of  $Fe^{3+}$  was set as 5% of total Fe based on the pelitic character of the sample and presence of ilmenite (e.g. Palin et al., 2016; Manzotti et al., 2018; Forshaw & Pattison, 2021). A pseudosection with no Fe<sup>3+</sup> is presented for comparison as the Supplementary Figure S1. Calculations in the range of 0–10% Fe<sup>3+</sup> show limited effect on phase assemblage fields. H2O was assumed to be present in excess, which is supported by the abundance of hydrous phases, particularly white mica and biotite. P–T pseudosections were calculated for the range of 0.5-1.0 GPa and 550-700°C. The following solution models were used in the calculations: garnet (White et al., 2007), biotite (White et al., 2014), white mica (White et al., 2014), plagioclase (Holland & Powell, 2003), ilmenite (White et al., 2000) and chlorite (White et al., 2014).

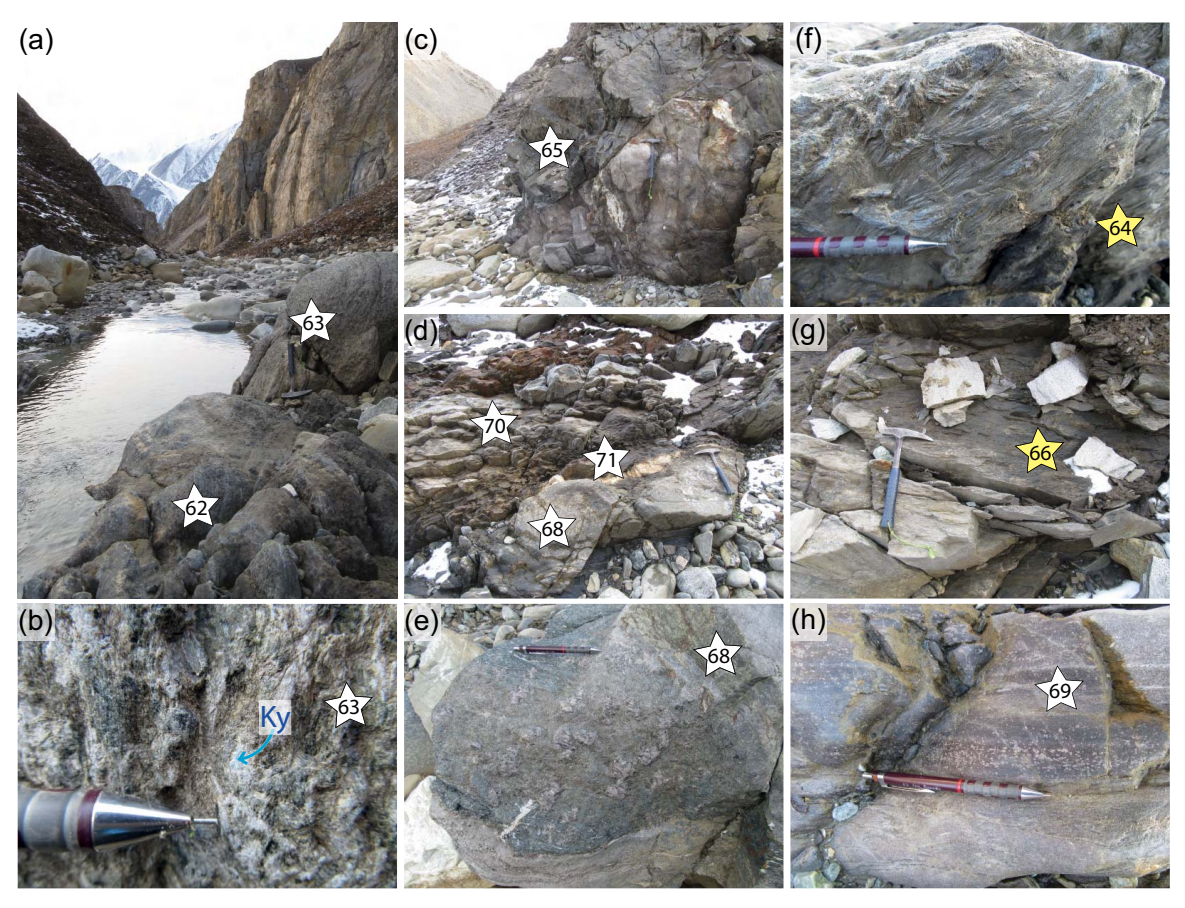


Fig. 3. Outcrop photographs of the Petersen Bay Assemblage; stars mark sample locations, yellow stars are samples studied in detail. (a) Amphibolite with kyanite viewed to the SW, (b) kyanite-bearing amphibolite, (c) lens of serpentinite, (d-e) garnet-bearing schist with megablasts (sample 17-68), metachert (17-70) and marble (17-61), (f) garbenschist, (g-h) garnet-bearing schists.

Table 1: Samples, locations and mineral assemblages

Sample ID	IGSN*	Lithology	Lat	Long	Grt	Amp	Ms	Bt	Pl	Qz	Ilm	Rt	Ку	St	Cal	Ser
17-10	IEMCC001C	Leucocratic dike	82° 13′ 25.7″	82° 37′ 50.9″			Х		Х	Х						
17-62	IEMCC002J	Amphibolite	82° 11′ 56.1″	82° 47′ 26.1″		X		Х	Х	X		Х	Х			
17-63	IEMCC002K	Amphibolite	82° 11′ 56.3″	82° 47′ 25.4″		X		Х	Х	X		Х	Х		Х	
17-64	IEMCC002L	Schist	82° 11′ 56.1″	82° 47′ 24.2″	X	X		Х	Х	X	X	Х	Х	Х		
17-65	IEMCC002M	Serpentinite	82° 11′ 57.0″	82° 47′ 16.8″												Х
17-66	IEMCC002N	Schist	82° 11′ 57.4″	82° 47′ 13.6″	X		X	Х	Х	X	X	Х	Х			
17-67	IEMCC002O	Schist	82° 11′ 57.6″	82° 47′ 13.9″												
17-68	IEMCC002P	Schist	82° 11′ 56.3″	82° 47′ 23.1″	X		X	Х	Х	X	X	Х			Х	
17-69	IEMCC002Q	Schist	82° 11′ 57.8″	82° 47′ 12.7″	X		Х	Х	Х	Х	Х					
17-70	IEMCC002R	Chert	82° 11′ 56.4″	82° 47′ 22.3″						X						
17-71	IEMCC002S	Limestone	82° 11′ 56.5″	82° 47′ 21.4″											Х	

<sup>\*</sup> IGSN - International Generic Sample Number

## Raman spectroscopy and elastic thermobarometry

Minerals commonly contain inclusions with significantly different elastic properties that can be used for elastic thermobarometry (Rosenfeld & Chase, 1961; Rosenfeld, 1969; Van der Molen & Van Roermund, 1986; Enami et al., 2007; Angel et al., 2014; Ashley et al., 2014; Kohn, 2014; Angel et al., 2015; Thomas & Spear, 2018; Murri et al., 2018). Elastic property differences between host and mineral inclusions can cause strain in the inclusion/host system that produces inclusions with remnant pressures. The remnant pressure in an inclusion can be related to its entrapment P-T conditions using equations of state and a physical model that describes volumetric changes to the inclusion-host mineral system. We calculated inclusion pressures (Pinc) from room temperature measurements of the 128, 206 and 464 cm<sup>-1</sup> Raman bands of strained quartz inclusions in garnet. Pinc was calculated using an elastic tensor approach, which is discussed in detail by Bonazzi et al. (2019) and Gonzalez et al. (2019). The

Table 2: Representative analyses of garnet

Sample ID	17-64	17-64	17-64	17-64	17-66	17-66	17-66	17-66
Text.type	Rim	Rim	Core	Core	Rim	Rim	Core	Core
Analysis	5	141	83	92	1	86	47	48
SiO <sub>2</sub>	38.63	38.65	38.31	38.44	37.26	37.64	36.97	37.55
TiO <sub>2</sub>	0.03	0.04	0.05	0.02	0.03	0.02	0.01	0.02
Al <sub>2</sub> O <sub>3</sub>	21.81	21.70	21.61	21.54	21.01	21.23	20.82	20.77
Cr <sub>2</sub> O <sub>3</sub>	0.01	0.05	0.06	0.06	0.01	0.02	0.00	0.00
FeO	27.38	27.40	24.62	24.71	36.13	34.32	32.06	32.09
MnO	2.40	2.19	6.03	5.87	1.01	0.81	4.77	4.75
MgO	7.29	6.80	6.20	6.44	2.78	3.55	2.34	2.35
CaO	2.96	3.27	3.43	3.20	2.49	3.26	3.11	2.86
Гotal	100.51	100.10	100.31	100.27	100.72	100.84	100.17	100.15
O	12	12	12	12	12	12	12	12
Si	2.994	3.008	2.993	3.001	2.988	2.990	2.989	3.018
Гi	0.002	0.002	0.003	0.001	0.002	0.001	0.001	0.001
Al	1.992	1.991	1.990	1.982	1.987	1.989	1.984	1.968
Cr	0.001	0.003	0.004	0.003	0.001	0.001	0.000	0.000
Fe	1.775	1.784	1.609	1.613	2.423	2.280	2.167	2.157
Mn	0.158	0.144	0.399	0.388	0.069	0.055	0.327	0.324
Mg	0.841	0.788	0.722	0.749	0.333	0.420	0.282	0.282
Ca	0.246	0.273	0.287	0.267	0.214	0.278	0.269	0.247
Cation total	8.010	7.993	8.007	8.005	8.016	8.014	7.994	8.016
X <sub>Alm</sub>	0.59	0.60	0.53	0.53	0.80	0.75	0.71	0.72
$X_{Sps}$	0.05	0.05	0.13	0.13	0.02	0.02	0.11	0.11
$X_{Prp}$	0.28	0.26	0.24	0.25	0.11	0.14	0.09	0.09
X <sub>Grs</sub>	0.08	0.09	0.10	0.09	0.07	0.09	0.09	0.08
X <sub>Fe</sub>	0.68	0.69	0.69	0.68	0.88	0.84	0.88	0.88

 $X_{Alm} = Fe^{2+}/(Fe^{2+} + Mg + Ca + Mn); X_{SDS} = Mn/(Fe^{2+} + Mg + Ca + Mn); X_{PD} = Mg/(Fe^{2+} + Mg + Ca + Mn); X_{GS} = Ca/(Fe^{2+} + Mg + Ca + Mn); X_{Fe} = Fe^{2+}/(Fe^{2+} + Mg); X_{Fe} = Fe^{2+}/(Fe^{2+} + Mg + Ca + Mn); X_{$ 

difference between the calculated shift of Raman bands and unstrained quartz ( $\Delta\omega$ ) was used for strain ( $\epsilon$ ) calculations in 'stRAinMAN software (Angel et al., 2019). We calculated stress ( $\sigma$ ) using the elastic tensor of quartz (Wang et al., 2015). The P<sub>inc</sub> was derived from the stresses following the equation:  $P_{inc} = -\frac{\sigma_1 + \sigma_2 + \sigma_3}{3}$ . We used software EoSFit-Pinc (Angel et al., 2017) to create entrapment isomekes.

We used  $\sim$ 150  $\mu$ m-thick doubly polished rock sections for Raman spectroscopic measurements at Syracuse University, Syracuse, NY, and 30  $\mu$ m-thick thin sections at Rensselaer Polytechnic Institute, Troy, NY. All inclusions measured were free of cracks, spherical and > 3 radii from any other interfaces (e.g. inclusions, polished surface, etc.). Raman spectra were measured on Bruker Senterra (Rensselaer Polytechnic Institute) and Renishaw in Via (Syracuse University) Raman microprobe spectrometers at room conditions of 1 bar (0.1 MPa) and 23°C. The spectrometers were calibrated against the Rayleigh scattered light from the 532 nm lasers, Ne lines and the 520.5 cm<sup>-1</sup> Raman band of a silicon standard. Throughout analytical sessions, we also measured the 128, 206 and 464 cm<sup>-1</sup> Raman bands of synthetic quartz crystals cut parallel to the c axis as reference materials. The laser was focused on the center of inclusions using 100× objectives (N.A.=0.9) to perform confocal measurements. The Raman shifted light (180° backscattering geometry) was dispersed with 1200 line/mm (Bruker) or 1800 line/mm (Renishaw) gratings onto charged-couple devices for 20 to

30 second analyses. We determined changes to the Raman band positions of quartz inclusions ( $\Delta\omega$ 128,  $\Delta\omega$ 206 and  $\Delta\omega$ 464) by measuring band positions in inclusions and subtracting the position of the same bands of a free quartz crystal (e.g. a piece of quartz reference material sitting on the Raman microscope stage).

## Monazite U-Pb geochronology and trace elements

Monazite U-Pb and trace element analysis was performed in-situ on polished thin sections using the Sensitive High-Resolution Ion Microprobe with Reverse Geometry (SHRIMP-RG) at the Stanford-USGS Micro-Analysis Center at Stanford University, CA. Back scattered electron (BSE) images of thin sections were collected using a Hitachi S-3400 N at the University of Iowa and a JEOL 5600 SEM at Stanford University. The thin sections were then cut and mounted together with natural reference materials in epoxy megamounts (37.5 mm diameter). The primary  $O_2^-$  ion beam was accelerated at 10 kV to achieve an intensity of 2.5-3.0 nA and focused to an  $18 \times 20 \mu m$  diameter spot. Pit depth was approximately  $\sim$ 2–3  $\mu$ m. The SHRIMP-RG was tuned for a mass resolution of  $\sim 8500$  (10% peak height), with the energy selection window set to accept high-energy ions into the collector in order to minimize transmission of low-energy, complex isobaric interferences (e.g.  $^{232}$ Th + REE+ $^{16}$ O++ or  $^{232}$ Th + REE+ $^{31}$ P++) and minimize the background at the Pb peak positions.

**Table 3:** Representative analyses of biotite, muscovite and amphibole

	17-64	17-64	17-66	17-66	17-66	17-66	17-66	17-64	17-64	17-64
Mineral	Biotite					Muscovite		Amphibol	e	
Text.type	Matrix	Matrix	Matrix	Matrix	Matrix	Matrix	Matrix	Core	Mantle	Rim
Analysis	49	51	12	7	18	11	25	17	26	37
SiO <sub>2</sub>	38.55	38.89	35.90	35.96	35.82	45.85	45.94	47.82	48.76	48.61
TiO <sub>2</sub>	1.23	0.97	2.09	2.23	1.59	0.67	0.76	0.14	0.08	0.12
$Al_2O_3$	18.26	17.98	18.90	18.78	19.01	36.78	35.91	13.79	12.05	12.29
Cr <sub>2</sub> O <sub>3</sub>	0.00	0.00	0.00	0.04	0.03	0.01	0.00	0.09	0.03	0.03
FeO	8.71	8.62	17.04	17.21	17.36	0.97	1.25	14.82	15.40	16.23
MnO	0.03	0.03	0.02	0.00	0.00	0.01	0.00	0.29	0.36	0.46
MgO	18.76	19.05	10.91	11.31	11.83	0.82	0.85	19.25	19.50	18.75
CaO	0.01	0.01	0.00	0.00	0.00	0.00	0.00	0.49	0.39	0.32
Na <sub>2</sub> O	0.59	0.50	0.38	0.38	0.37	1.55	1.36	1.30	1.30	1.18
K <sub>2</sub> O	8.46	8.29	9.26	9.40	8.69	9.54	9.54	0.01	0.00	0.02
BaO	0.10	0.16	0.05	0.00	0.10	0.21	0.15	n.a.	n.a.	n.a.
F	0.06	0.19	0.17	0.23	0.31	0.01	0.04	0.00	0.00	0.00
Cl	0.01	0.02	0.00	0.01	0.00	0.00	0.00	0.00	0.00	0.00
Total	94.77	94.71	94.73	95.55	95.12	96.43	95.80	98.00	97.87	97.99
0	11	11	11	11	11	11	11	22	22	22
Si	2.778	2.804	2.720	2.707	2.703	3.012	3.039	6.665	6.821	6.822
Ti	0.067	0.053	0.119	0.126	0.090	0.033	0.038	0.015	0.008	0.014
$Al^{IV}$	1.222	1.196	1.280	1.293	1.297	0.988	0.961	1.335	1.179	1.178
$Al^{VI}$	0.329	0.331	0.407	0.372	0.393	1.859	1.839	0.931	0.807	0.855
Cr	0.000	0.000	0.000	0.002	0.002	0.001	0.000	0.009	0.004	0.003
Fe <sup>3+</sup>	0.000	0.000	0.000	0.000	0.000	0.000	0.000	0.430	0.423	0.367
Fe <sup>2+</sup>	0.525	0.519	1.080	1.084	1.096	0.053	0.069	1.298	1.379	1.538
Mn	0.002	0.002	0.002	0.000	0.000	0.000	0.000	0.035	0.042	0.054
Mg	2.015	2.047	1.232	1.269	1.331	0.080	0.084	4.000	4.067	3.923
Ca	0.001	0.001	0.000	0.000	0.000	0.000	0.000	0.074	0.058	0.048
Na	0.082	0.070	0.056	0.056	0.055	0.197	0.175	0.353	0.351	0.320
K	0.777	0.762	0.895	0.903	0.837	0.799	0.805	0.000	0.000	0.000
Ва	0.003	0.004	0.002	0.000	0.003	0.005	0.004	n.a.	n.a.	n.a.
Total	7.800	7.789	7.793	7.812	7.806	7.029	7.014	15.145	15.139	15.122
$X_{Fe}$	0.21	0.20	0.47	0.46	0.45			0.24	0.25	0.28

 $X_{Fe} = Fe^{2+}/(Fe^{2+} + Mg)$ 

Repeated analysis of reference material 44 069 monazite (Concordia age =  $424.9 \pm 0.5$  Ma; Aleinikoff et al., 2006) was used to calculate ages of unknowns. Trace element concentrations (Y, REE, U, Th) were calibrated using 44 069 values established through comparison with trace element concentrations of reference material NAM monazite (Aleinikoff et al., 2012). The estimated uncertainty ( $1\sigma$  SD) for monazite trace element concentrations is 3 to 6% for U, Th, Y, La, Pr, Nd, Sm, Eu, Gd, and Dy and  $\sim$ 10% for Er and Yb based on repeated analysis of 44 069 and reported reproducibility of NAM (Aleinikoff et al.,

Data processing and plotting was performed using Squid 2.51 and Isoplot 4.15 (Ludwig, 2009, 2012). Corrections for common Pb using compositional estimates from Stacey & Kramers (1975) were based on <sup>207</sup>Pb for <sup>206</sup>Pb/<sup>238</sup>U ages and the measured <sup>204</sup>Pb for <sup>207</sup>Pb/<sup>206</sup>Pb ages. Isotopic ratios and dates are reported with analytical uncertainties ( $2\sigma$ ). The  $^{206}\text{Pb}/^{238}\text{U}$  and  $^{207}$ Pb/ $^{206}$ Pb model ages are reported with  $2\sigma$  uncertainties that include error in external reproducibility (1 $\sigma$  SD) of reference material 44 069 during the individual analytical session summed in quadrature.

#### **RESULTS**

## Petrography and chemistry

Thirty thin sections of the PBA were carefully examined and the mineral assemblages for samples from the studied outcrop are given in Table 1. Bulk and trace element chemistry for selected samples is presented in Table S1. Amphibolite containing kyanite and staurolite has been classified as high-Al metabasite in the literature (e.g. Helms et al., 1987). The kyanite-amphibolite in the PBA falls short of the criteria for high-Al basalts given by Crawford et al. (1987), i.e. SiO<sub>2</sub> < 54 wt % and  $Al_2O_3 > 16.5$  wt %, although sample 17-62 is close with  $SiO_2 = 55.16$  wt % and  $Al_2O_3 = 16.37$ %. Garbenschist sample 17-64 has a very similar bulk composition as garbenschist 88E1118 studied by Klaper & Ohta (1993). Garbenschist samples 17-64 and 17-62 are characterized by SiO<sub>2</sub> of 57.70 and 59.09 wt %, Al<sub>2</sub>O<sub>3</sub> of 13.97 and 15.05 wt %. The two garnet-bearing schists (17-64 and 17-66) that contain monazite, and are thus suitable for petrochronology, are described below. Tables 2–4 present representative analyses of their mineral chemistry.

Garbenschist 17-64 is composed of garnet, biotite, amphibole, staurolite, kyanite, plagioclase and quartz

Table 4: Representative analyses of plagioclase and staurolite

Sample ID	17-64	17-64	17-66	17-66	17-66	17-64	17-64
Mineral	Plagioclase					Staurolite	
Text.type	Matrix	Matrix	Core	Rim	Rim	Core	Rim
Analysis	38	48	7	17	18	11	13
SiO <sub>2</sub>	60.70	61.42	61.60	64.04	63.07	28.52	28.27
TiO <sub>2</sub>	0.00	0.04	0.00	0.00	0.02	0.69	0.50
Al <sub>2</sub> O <sub>3</sub>	25.24	25.06	24.14	23.55	23.84	53.96	53.77
Cr <sub>2</sub> O <sub>3</sub>	n.a.	n.a.	n.a.	n.a.	n.a.	0.31	0.30
FeO	0.10	0.50	0.07	0.04	0.01	9.82	10.48
MnO	0.00	0.00	0.00	0.00	0.00	0.13	0.13
MgO	0.00	0.02	0.00	0.00	0.00	3.31	2.96
CaO	6.79	5.74	5.46	3.94	4.76	0.00	0.01
Na <sub>2</sub> O	7.21	7.46	7.74	8.45	8.12	0.07	0.07
K <sub>2</sub> O	0.02	0.16	0.51	0.10	0.04	0.01	0.01
ZnO	n.a.	n.a.	n.a.	n.a.	n.a.	1.43	1.46
Total	100.05	100.39	99.53	100.13	99.86	98.25	97.96
0	8	8	8	8	8	23	23
Si	2.692	2.713	2.743	2.811	2.782	3.899	3.890
Ti	0.000	0.001	0.000	0.000	0.001	0.071	0.052
Al	1.320	1.305	1.267	1.219	1.240	8.695	8.720
Cr	0.000	0.000	n.a.	n.a.	n.a.	0.033	0.032
Fe	0.004	0.019	0.003	0.002	0.001	1.123	1.206
Mn	0.000	0.000	0.000	0.000	0.000	0.015	0.015
Mg	0.000	0.001	0.000	0.000	0.000	0.675	0.607
Ca	0.323	0.272	0.260	0.185	0.225	0.000	0.001
Na	0.620	0.639	0.669	0.719	0.695	0.019	0.019
K	0.001	0.009	0.029	0.005	0.002	0.002	0.001
Zn	0.000	0.000	n.a.	n.a.	n.a.	0.144	0.148
Cation total	4.959	4.957	4.972	4.942	4.946	14.676	14.692
X <sub>Ab</sub>	0.66	0.69	0.70	0.79	0.75		
X <sub>An</sub>	0.34	0.30	0.27	0.20	0.24		
X <sub>Or</sub>	0.00	0.01	0.03	0.01	0.00		
$X_{Fe}$						0.57	0.61

 $X_{Fe} = Fe^{2+}/(Fe + Mg)$ ;  $X_{Ab} = Na/(Na + Ca + K)$ ;  $X_{An} = Ca/(Na + Ca + K)$ ;  $X_{Or} = K/(Na + Ca + K)$ .

(Fig. 4). The accessory phases are zircon, monazite, allanite, xenotime, apatite, tourmaline, pyrite, ilmenite and rutile. Garnet forms anhedral porphyroblasts up to 5 mm in diameter and is not abundant (i.e. 1-2 porphyroblasts at the thin section scale; Fig. 4a and b). The porphyroblasts have abundant inclusions of quartz, ilmenite, pyrite and allanite. Garnet rims are partly replaced by plagioclase and biotite. Garnet exhibits prograde zoning, which is demonstrated by bell-shaped spessartine component, varying from 0.14 in the core to 0.05 mol % in the rim (Fig. 5).  $X_{Fe} = Fe^{2+}/Fe^{2+} + Mg$ decreases from core to rim. Grossular is rather constant at ~0.09 mol % throughout the garnet porphyroblast. Back diffusion is observed in the garnet rim (Fig. 5), which results in an increase of  $X_{Sps}$  and  $X_{Fe}$  in the outer rim. The preferred shape orientation of biotite defines the main schistosity. Biotite has  $X_{Fe} = Fe^{2+}/Fe^{2+} + Mg$  ranging from 0.20 to 0.21 and low Ti between 0.05-0.07 a.p.f.u (atoms per formula unit). Plagioclase is mostly sodic and characterized by Ab = 66-70%, An = 30-34% and Or = 0-1%. Amphibole grew over the foliation and developed typical garben texture (Fig. 4c), forming randomly oriented, feather-like neoblasts up to 5 cm long. Amphibole is gedrite according to the classification of Hawthorne et al. (2012), with Si = 6.42-7.02 a.p.f.u. and moderate to

low Na = 0.27-0.36 a.p.f.u.  $X_{Fe} = Fe^{2+}/Fe^{2+} + Mg$  is slightly zoned and varies from 0.24 to 0.26. Amphibole is partly replaced by chlorite and biotite, and cut by veins that formed during late fluid influx (Fig. 4c). Staurolite remnants in the matrix (Fig. 4d) are ferrous ( $X_{Fe} = 0.63$ -0.67) and characterized by Zn ranging from 0.14-0.17 a.p.f.u.; Zn is higher near the rims. Kyanite is found in the matrix, often showing resorbed rims (Fig. 4e) or helicitic texture. Ilmenite, partially replaced by rutile, is abundant in the matrix and as inclusions in garnet.

Metapelite 17-66 has a well-developed foliation marked by biotite and white mica (Fig. 6a), and consists of garnet, biotite, muscovite, plagioclase, quartz and kyanite. Accessory minerals are zircon, monazite, allanite, xenotime, apatite, tourmaline, ilmenite and rutile. The sample contains almost no sign of retrogression. Garnet is ~1−2 mm in diameter and forms subhedral porphyroblasts surrounded by matrix minerals (Fig. 6a, b and c). Garnet cores are inclusion-rich, while rims are rather inclusion free. The inclusions are mostly quartz, ilmenite, zircon, apatite and allanite; no kyanite was observed in the garnet. Garnet shows prograde growth zoning and is generally almandine rich (Fig. 7). Spessartine has a bell-shaped profile with a decrease of  $X_{Sps}$  from 0.11 to 0.02 mol % towards the rim. A

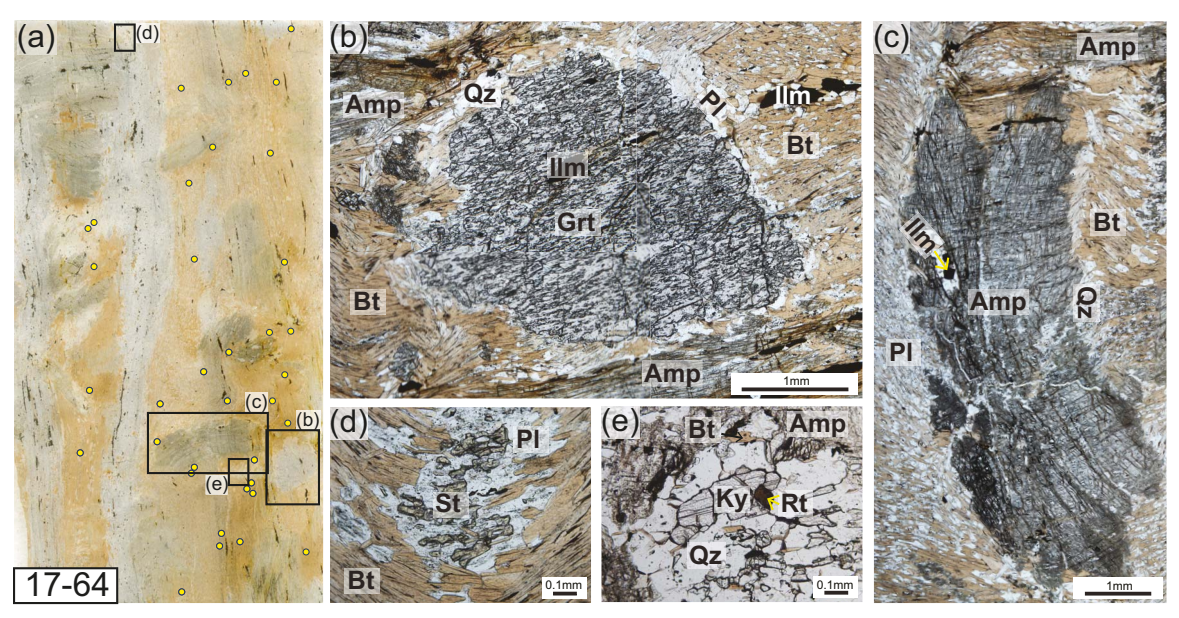


Fig. 4. Photomicrographs from garbenschist sample 17-64 in plane-polarized light (PPL). (a) Thin section scan; brown areas are biotite rich, dots are monazite locations, (b) garnet porphyroblast overgrowing schistosity, (c) amphibole overgrowing the crenulated foliation, (d) relict of staurolite, (e) kyanite in the matrix.

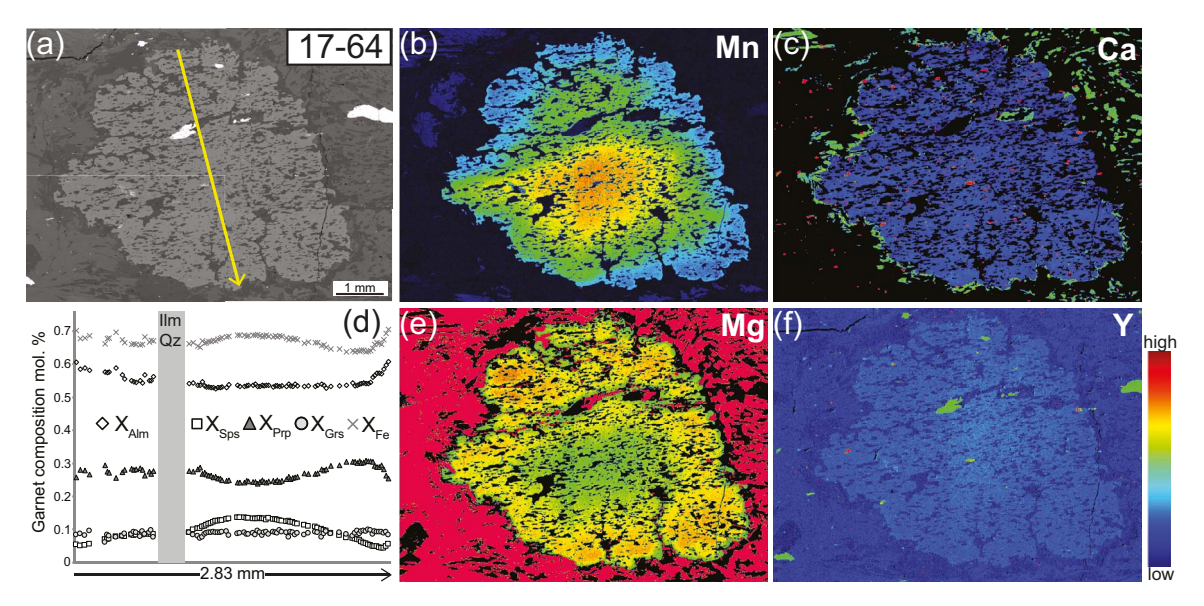


Fig. 5. Chemistry of a garnet in sample 17-64. (a) Back-scattered electron (BSE) image, (d) compositional profile along the transect marked on the BSE image, (b,c,e,f) Mn, Mg, Ca and Y compositional maps of garnet.

small increase of  $X_{Sps}$  (<0.01 mol %) is observed in the outer rim. X<sub>Fe</sub> varies from 0.88 in the core to 0.84; it increases slightly in the outer rim (up to 0.88). Grossular is characterized by higher values in the core (up to 0.09) and depletion in the rim ( $\sim$ 0.06). The grossular X-ray map demonstrates calcium diffusion along the bigger quartz inclusions (Fig. 7). Up to 0.26 mol % Y is concentrated in the garnet core and decreases below the detection limit in the mantle and rim. Very thin,  $\sim$ 1–2  $\mu$ m, Y-rich annuli occur in the garnet rims (Fig. 7). Biotite defines the foliation, commonly forming intergrowths with white mica (Fig. 6d). Biotite is compositionally homogenous with  $X_{Fe} = 0.45-0.47$  and Ti = 0.09-0.13 a.p.f.u. White mica is muscovite with Si = 3.01-3.04 a.p.f.u. and Na varying from 0.17-0.20 a.p.f.u. Plagioclase, mostly sodic, is slightly zoned with a composition of Ab<sub>70-79</sub>An<sub>17-30</sub>Or<sub>0-5</sub>. Kyanite forms grains up to 0.5 mm long that lie parallel or slightly oblique to the foliation (Fig. 6c). Kyanite rims are rarely replaced by sericite. Ilmenite is a common phase in the garnet and matrix. Ilmenite in the garnet rim and in the matrix is partly replaced by rutile (Fig. 6e).

## Thermodynamic modeling

Phase equilibria modeling (i.e. pseudosections) could not be applied to most of the PBA samples. Garnetbearing schists typically contain late calcite and amphibole overgrowing the metamorphic fabrics, making it impossible to define the bulk composition representing

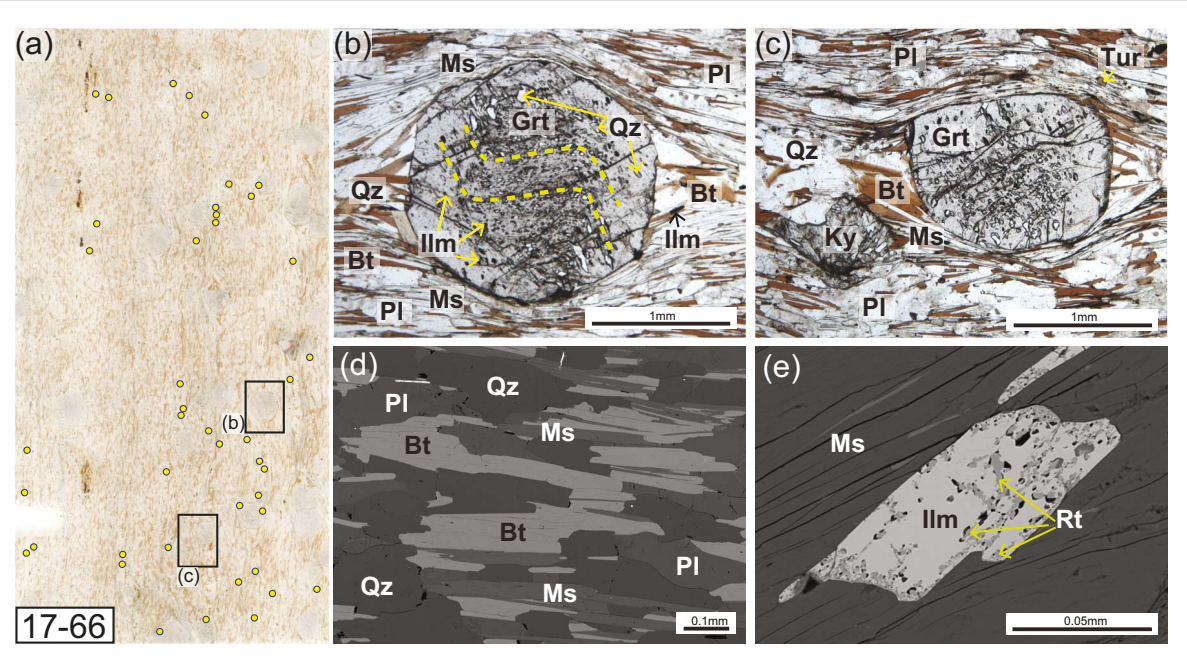


Fig. 6. PPL photomicrographs and BSE images from metapelite 17-66. (a) Thin section scan, dots are monazite locations, (b) garnet porphyroblast with inclusion trails marked in yellow, (c) kyanite and garnet porphyroblasts are oblique to the main foliation, (d) shape preferred orientation of biotite and muscovite define the foliation, (e) rutile replacing matrix ilmenite.

the conditions of equilibrium. Only garnet-mica schist 17-66, a typical metapelite, is suitable for pseudosection modeling because it contains the least altered mineral assemblage and shows no direct evidence of late fluid influx. The P-T conditions of growth of the garnet core were estimated using compositional isopleths. The intersecting isopleths plot in the stability field of biotite + garnet + plagioclase + white mica + ilmenite + chlorite + quartz at c. 0.76-0.82 GPa and 585-600°C (Fig. 8a). A second pseudosection was calculated based on the effective bulk composition obtained by subtracting the garnet core composition from the whole rock chemistry (e.g. Evans, 2004; Lanari & Engi, 2017). The modal proportion of garnet core (2.5%) was estimated using image analysis in ImageJ software. The isopleths of grossular from the garnet rim were compared with isopleths of X<sub>Fe</sub> in biotite and Si number in white mica. The modelled isopleths intersect at ~0.79-0.85 GPa and 650-665°C in the stability field of biotite + garnet + plagioclase + white mica + kyanite + rutile + quartz ± ilmenite (Fig. 8b). These peak P-T conditions represent garnet rim formation and the mineral assemblage is in agreement with petrographic observations.

## QuiG thermobarometry

Garnet in both samples contains abundant quartz inclusions. The inclusions are mostly concentrated in the cores of garnet crystals (Fig. 6b-c, 7). All inclusions chosen for Raman measurements were spherical, 5–30  $\mu m$ in diameter (Fig. 9b-c) and isolated from any interfaces (see Methods). Inclusions with visible cracks or defects were avoided. Forty-four quartz inclusions in garnet were measured in metapelite 17-66 (Table S2). The repeatable

measurements of reference quartz give stable errors on the 128, 206 and 464 cm<sup>-1</sup> Raman bands. Quartz inclusions from sample 17-66 give an average Pinc of  $0.24 \pm 0.08$  GPa (Table S2, Fig. 9). The anisotropy (A) varies from -0.002 to -0.045, but calculated isomekes give consistent pressures of entrapment.

A number of authors have combined QuiG thermobarometry with inclusion trace element thermometry (e.g. Zirconium-in-rutile: Castro & Spear, 2017; Wolfe & Spear, 2018; Harvey et al., 2021; Titanium-in-quartz: Gonzalez et al., 2019); however, the PBA rocks are not suitable for this approach. Rutile forms thin ( $<2 \mu m$ ) intergrowths with ilmenite (Fig. 6e) that are too small for microprobe analysis. The chemical equilibrium between rutile intergrowths and zircon, and between quartz and rutile, and their associations with garnet collectively complicate using the crossing points of QuiG isomekes with Ti-in-quartz and/or Zr-in-rutile isopleths for thermobarometry. Thus, the QuiG data have been combined with conventional thermobarometry to estimate the P–T conditions. Ti-in-biotite thermometry (Henry et al., 2005) gives reliable estimates for amphibolite facies rocks (e.g. Palin et al., 2012). The Ti-in-biotite thermometry for sample 17-66 intersects with the average QuiG isomeke at 0.7-0.9 GPa and 540-600°C (Fig. 9a). Results from the geothermometer garnet-biotite (GB, Hodges & Spear, 1982) and geobarometer GASP (Hodges & Spear, 1982) are shown for comparison (Fig. 9a), since they are commonly used in metapelites. The lowest  $X_{Fe}$ in biotite was paired with the highest X<sub>Fe</sub> in garnet and the highest  $X_{\text{Fe}}$  in biotite was combined with the lowest X<sub>Fe</sub> in garnet to provide the possible range of temperatures. GASP was applied to the garnet rim, matrix biotite and plagioclase because kyanite occurs

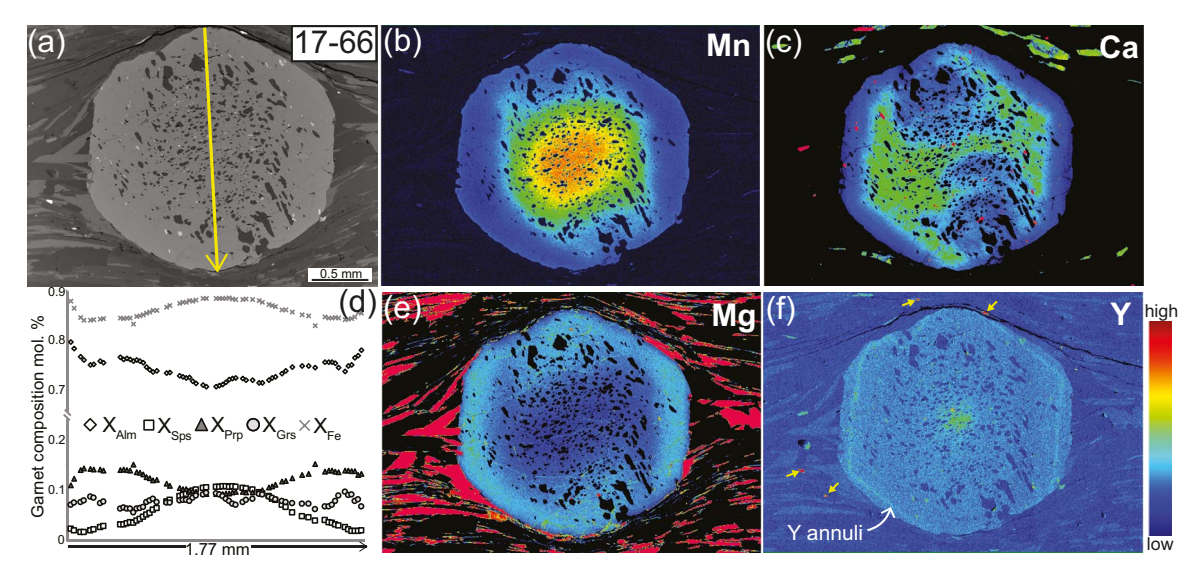


Fig. 7. Chemical zoning of a garnet in metapelite 17-66. (a) BSE image, (d) compositional profile shown on the BSE image, (b,c,e,f) X-ray maps of garnet for Mn, Mg, Ca and Y. Yellow arrows on Y map indicate monazite grains.

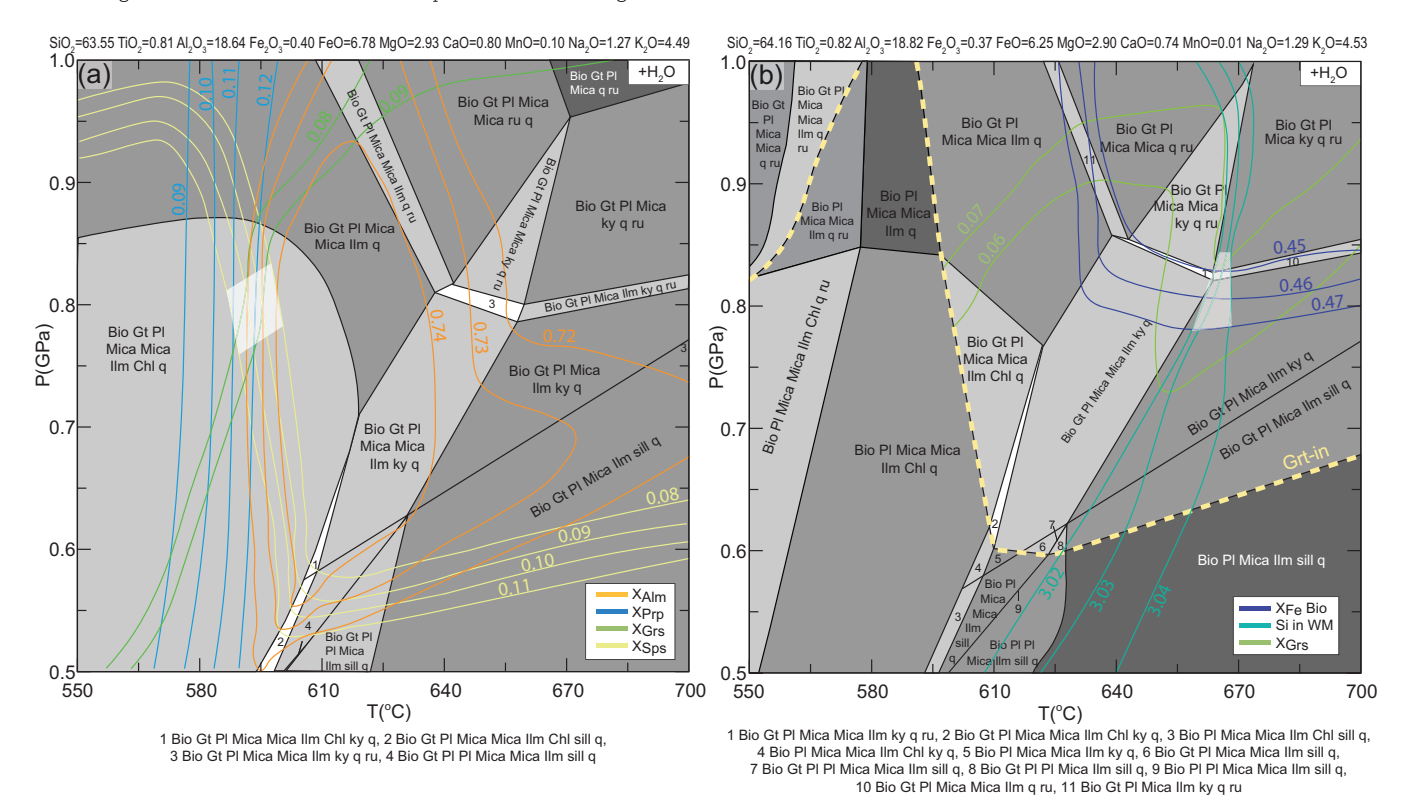


Fig. 8. P-T pseudosections for metapelite 17-66. (a) garnet cores (b) garnet rims (based on the effective bulk composition). Colored lines show constant composition for indicated mineral components. Light gray rhombs are the estimated conditions of core and rim growth.

only in the matrix (Fig. 6c) and there is no textural evidence for kyanite growth together with the garnet core. GB is consistent with Ti-in-biotite results, but yields a wider spread of temperature ranging from 450° to 600°C. The GB thermometer coupled with the GASP barometer gives the results of ~600°C at 0.85 GPa. Representative biotite composition and QuiG data used for calculations are given in Tables 3 and S2, respectively.

We applied a similar procedure to garbenschist 17-64. Quartz inclusions (n = 30) were measured in two garnets. Pinc calculated for the measured inclusions gives an average  $P_{inc}$  of 0.17  $\pm$  0.02 GPa (A = -0.022-0.003). The Tiin-biotite thermometry together with the average QuiG isomekes estimates P-T conditions at 0.7-0.8 GPa and 480-520°C (Fig. 9a). GB yields a wide temperature range of 440° to 530°C. GB coupled with GASP barometry displays lower P-T conditions of ~540°C at 0.66 GPa.

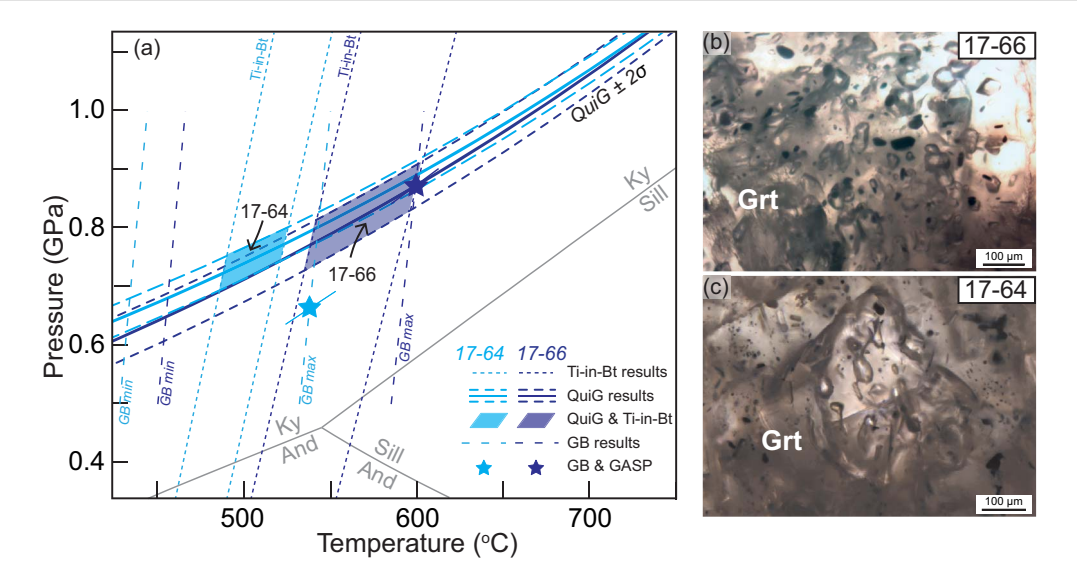


Fig. 9. (a) P-T diagram with QuiG, Ti-in-biotite (Ti-in-Bt), garnet-biotite (GB) and GASP results shown for sample 17-66 and 17-64, (b) and (c) representative PPL photomicrographs showing abundant quartz inclusions in garnet.

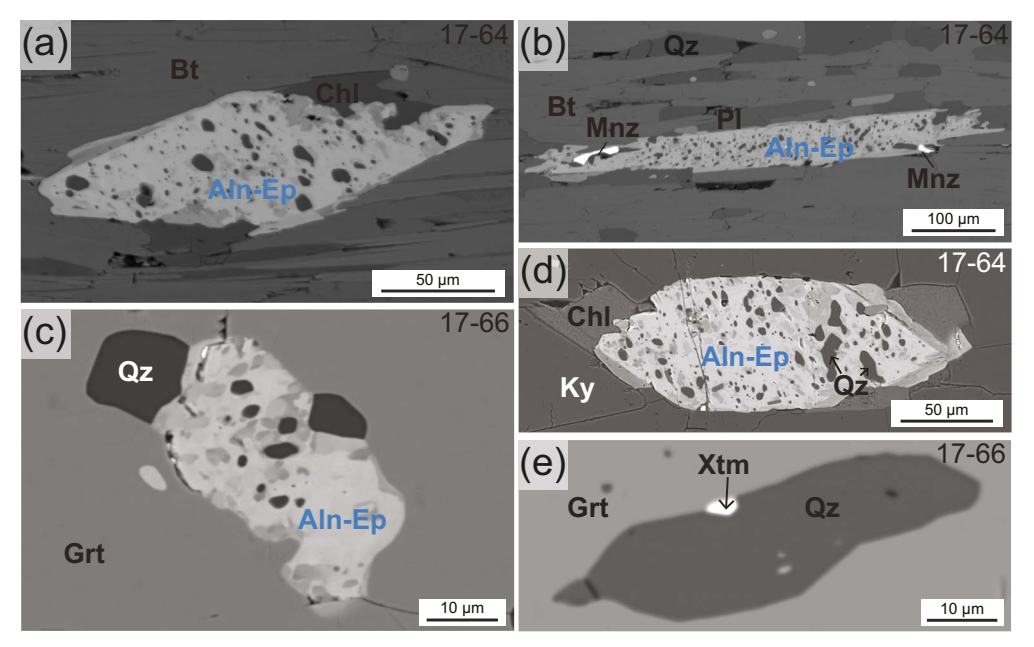


Fig. 10. BSE images showing relationships among REE-bearing phases allanite, epidote, monazite and xenotime.

# REE phase relationships and monazite petrochronology

Sample 17-64 contains the REE bearing minerals xenotime, allanite and monazite. Xenotime occurs as small grains (<5  $\mu$ m) in the garnet and in the matrix. Allanite forms inclusion-rich grains up to 500  $\mu$ m long in the matrix (Fig. 10a and b). The inclusions are mostly quartz. Allanite is typically replaced by epidote (Fig. 10a and b) with rare overgrowths of microcrystalline monazite (Fig. 10b). Allanite also occurs as inclusions within garnet and kyanite (Fig. 10d). Monazite forms small (<30  $\mu$ m) grains that occur only in the matrix (Fig. 11). Apatite is a common accessory mineral both in the matrix and in the garnet.

Xenotime, monazite and allanite are the REE bearing phases in sample 17-66. Xenotime occurs as inclusions

<5  $\mu$ m in diameter within high-Y garnet cores (Figs 7 and 10e). Allanite forms aggregates breaking down to REEenriched epidote and apatite, occurring as metastable matrix grains or as inclusions in the garnet core (Fig. 10c). Monazite occurs as inclusions in garnet rims (<30  $\mu$ m) or as grains in the matrix (<50  $\mu$ m). Representative monazite grains are shown in Fig. 12.

Monazite in garbenschist 17-64 is chemically zoned with three recognizable domains. The dominant trend shows Th and Y decreasing between populations I-III (Fig. 13). Thorium concentration varies between 15 480 and 53 772 ppm, whereas Y ranges from 10 780-17 150 ppm (Fig. 13b, Table 5). The trace element signature is consistent within monazite domains and shows enrichment in LREE, slight depletion in HREE and a moderate negative Eu anomaly (Eu\* = 0.19 to 0.31;

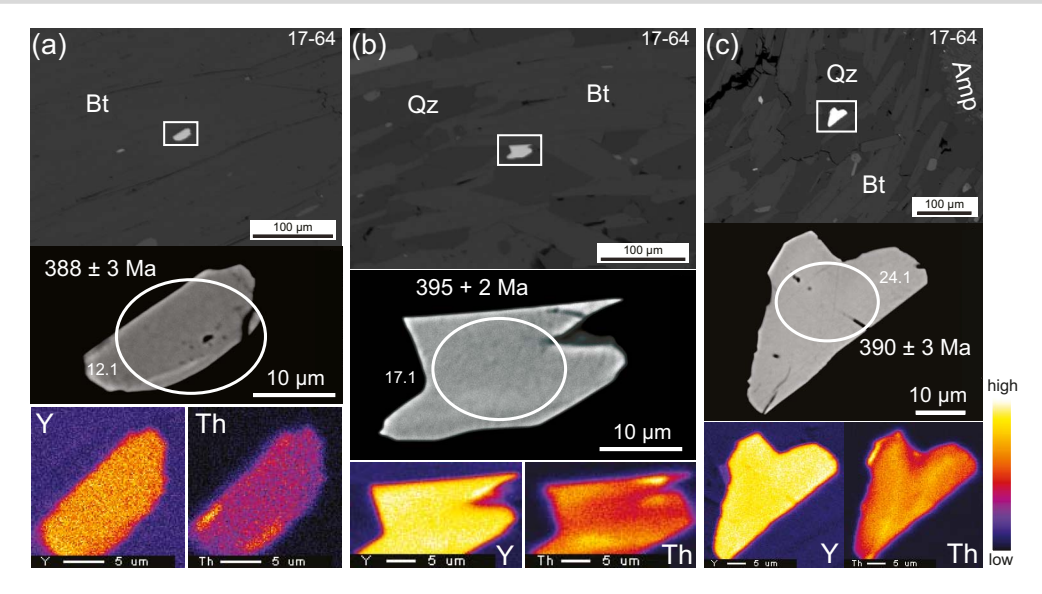


Fig. 11. BSE images, Th and Y X-ray chemical maps of selected monazite grains from garbenschist 17-64. Ellipses indicate analytical spots for U/Pb and trace elements collected with SHRIMP-RG.

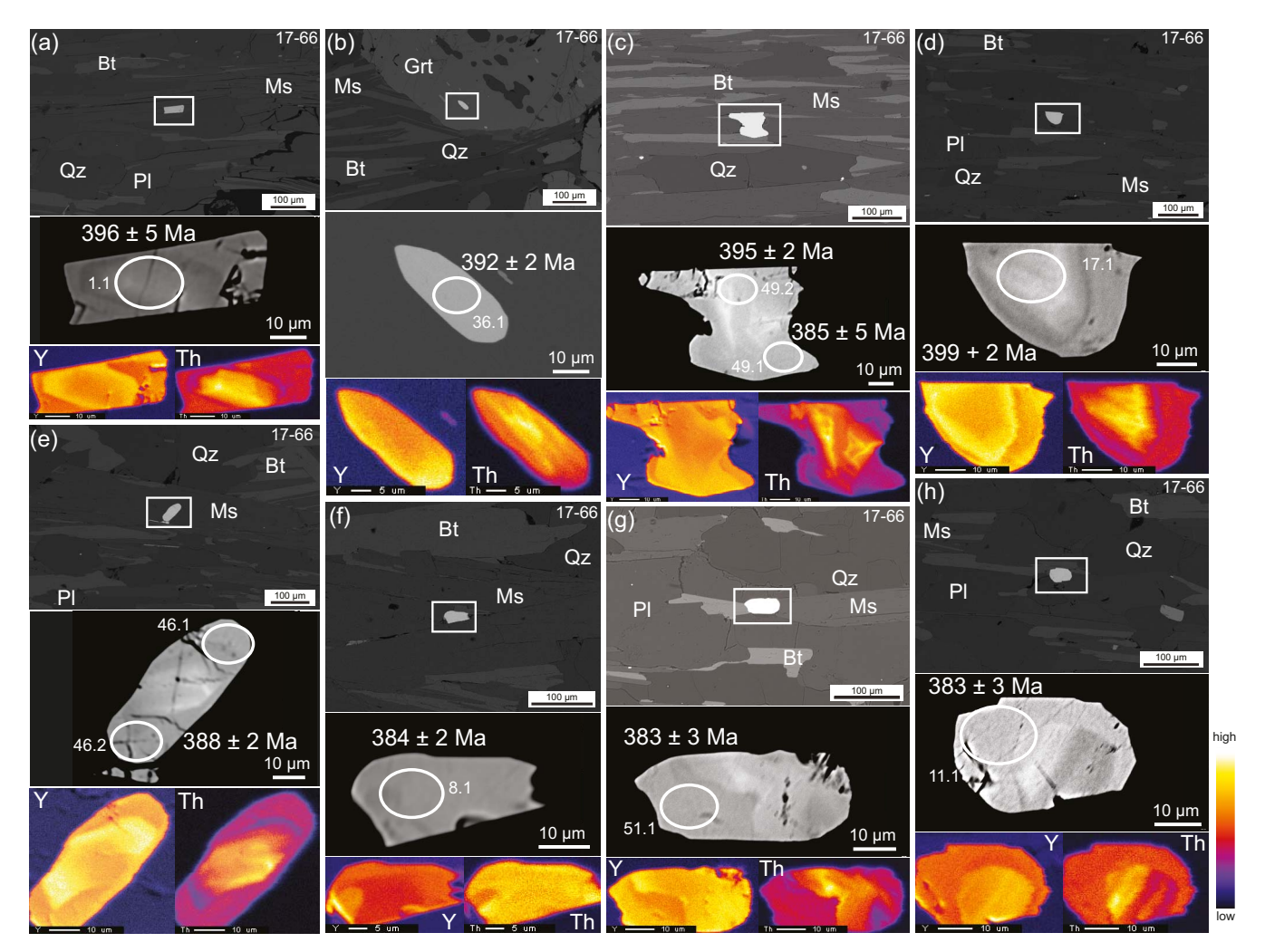


Fig. 12. BSE images, Th and Y compositional maps of representative monazite grains from metapelite 17-66. Ellipses indicate analytical spots for U/Pb and trace elements.

Fig. 13a, Table 5). Monazite-I defines a weighted mean  $^{206}$ Pb/ $^{238}$ U age of  $394 \pm 2$  Ma (n = 11, MSWD = 0.6, Fig. 14a, Table 6) and is characterized by high/moderate Th

(21 025-53 773) and Y (12 863-17 150) contents. Monazite-II yields the age of  $388 \pm 2$  Ma (n=7, MSWD=0.8,Fig. 14a). Monazite-II gives moderate Th (18073-42397)

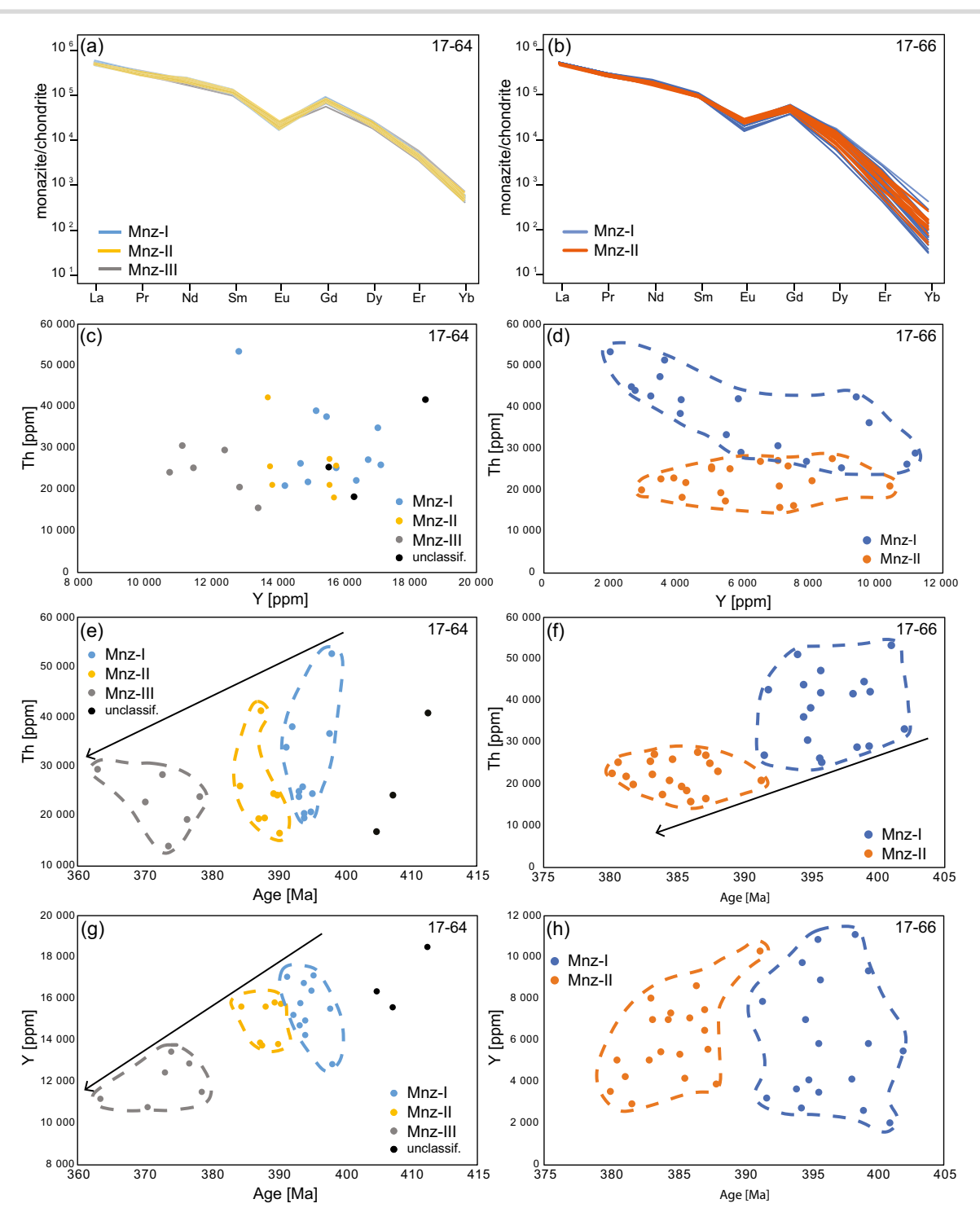


Fig. 13. Chemistry of monazite from samples 17-64 and 17-66. (a), (b) Chondrite-normalized REE patterns (Sun & McDonough, 1989); (c), (d) Y vs Th binary diagram; (e), (f) age vs Th binary diagram; (g), (h) age vs Y binary diagram. Points excluded from age calculations are not included on Fig. 13: sample 17-64: 7.1, 13.1, 14.1, 18.1, 25.1; sample 17-66: 10.1, 46.1, 54.1 Black dots are unclassified analyses which are most probably mixed analyses.

and Y (13775–15833). A younger age of  $374\pm6$  Ma is recorded by a more scattered Monazite-III population (n=6, MSWD=3.1, Fig. 14a). Monazite-III yields lower Th (15480–30698) and Y (10782–13457) compared to other populations. Three older (> 400 Ma) monazite dates are reported and are interpreted as a mixed age between the detrital monazite core and the metamorphic rim.

Monazite in metapelite 17-66 is chemically zoned with distinct cores and rims. Two domains were defined based on high-contrast BSE images and X-ray maps (Fig. 12). Domain I (Monazite-I) corresponds to high Th (25 077–53 285 ppm) and moderate Y (2 029–11 191 ppm) (Fig. 12f, Table 5). Monazite-I occurs within garnet rims (Fig. 12b) or forms cores of matrix monazite (Fig. 12a, c, d, e and g). Monazite-II is characterized by

Downloaded from https://academic.oup.com/petrology/article/63/8/egac068/6650310 by University of Iowa user on 24 August 2022

			spor	, -	u,	, ,	, רמ	Į,	DN.	E ,	Eu ,	ğ ,	δ,		Yb ,
		location	location	(mdd)	(mdd)	(mdd)	(mdd)	(mdd)	(mdd)	(mdd)	(mdd)	(mdd)	(mdd)	(mdd)	(mdd)
Sample 17-66															
Monazite-I	1766-01.1	Matrix	Core	2974	41 770	5878	114 050	27 227	86324	14694	1143	10234	2710	186	12
	1766-03.1	Matrix	Rim	2256	29 010	5898	118 191	25 424	82778	13881	1429	9776	2718	193	16
	1766–13.1	Matrix	Core	2774	36 069	9823	115 148	27 247	81261	14245	1492	11539	4011	432	45
	1766–17.1	Matrix	Core	3038	44 653	2642	121 549	26 771	86582	14035	1130	8163	1435	87	9
	1766–18.1	Matrix	Core	2675	33 120	5517	120315	26 904	87 854	14606	1442	10179	2567	162	12
	1766–19.1	Matrix	Core	3297	47 236	3518	118732	27 717	88 107	14625	1273	9440	1896	108	∞
	1766 - 20.1	In garnet	Core	1792	25 077	8968	120416	26 303	85 270	14 234	1612	10632	3755	286	21
	1766-21.1	Matrix	Core	2901	43 820	2776	120525	27 293	81373	12772	1006	7539	1485	78	2
	1766-30.1	Matrix	Core	2052	26 812	7914	121885	26 603	88 456	14 533	1605	10364	3407	219	16
	1766–31.1	Matrix	Core	3311	42 209	9413	117 340	27 407	96420	16263	1466	11584	3804	339	26
	1766–36.1	In gamet	Core	3159	42 563	3244	121 346	27 226	84959	13218	927	7260	1494	86	∞
	1766–39.1	Matrix	Core	3416	51 138	3660	120 346	27 952	88 784	14250	1093	8300	1853	135	11
	1766-41.1	Matrix	Core	2524	30 390	7052	118 583	27 656	86204	14422	1389	10327	3069	202	14
	1766-42.1	In garnet	Core	2102	28 672	11 191	111615	26 224	81 597	13818	1403	9525	4163	447	69
	1766-45.1	Matrix	Core	1932	25 936	10 954	116391	26 407	82 529	14116	1576	10736	3907	315	23
	1766-48.1	Matrix	Core	3188	53 285	2029	119082	27 479	82 999	12 994	837	7176	1112	29	2
	1766-49.2	Matrix	Core	2764	38 284	4132	116014	25 453	90 273	14 789	1333	9309	2088	133	10
	1766-50.1	Matrix	Core	3052	41573	4141	120176	26 913	87 033	14 261	1128	8974	2067	152	11
Monazite-II	1766-02.1	Matrix	Core	1849	20 714	10376	116244	25 241	83415	14123	1484	10841	4049	338	28
	1766-07.1	Matrix	Core	1974	15 587	7121	118777	25 243	83 695	13952	1607	10513	3113	238	24
	1766-08.1	Matrix	Core	1787	17 102	5480	120 409	25 977	76170	12619	1306	9084	2445	179	17
	1766–11.1	Matrix	Rim	2381	26 939	7053	117 667	26 763	82 969	14329	1462	11379	3241	284	44
	1766–14.1	Matrix	Rim	2422	20 723	7052	114 905	25 645	83 311	14171	1458	10366	3113	307	46
	1766–22.1	Matrix	Core	1481	16 146	7541	121459	25 452	87 059	14391	1616	10752	3520	207	13
	1766-23.1	Matrix	Core	2069	24 837	5621	121064	26 738	85 731	14 372	1506	10516	2810	189	18
	1766–26.1	Matrix	Core	2192	22 430	3553	121215	25 494	87 481	14 390	1397	6266	2013	126	20
	1766-27.1	Matrix	Core	2317	26 609	6536	118088	26 888	88 934	15258	1619	11474	3135	245	28
	1766–28.1	Matrix	Core	1824	19 134	5348	120 759	26293	81686	13522	1419	6996	2495	175	18
	1766–34.1	Matrix	Core	1815	18 085	4190	118034	25 707	84307	13678	1509	9273	2188	105	6
	1766–35.1	Matrix	Core	2415	27 439	8695	119 101	26 605	83 827	14115	1527	10517	3536	278	25
	1766–37.1	Matrix	Rim	1989	21 518	4282	118 251	26 355	85 220	14231	1454	10323	2241	137	21
	1766-40.1	Matrix	Core	1709	19 776	2951	118649	25 024	81 535	13 106	1396	8581	1662	83	∞
	1766–46.2	Matrix	Rim	2160	22 819	3922	116700	25 807	85 588	14200	1463	9391	1933	122	17
	1766-49.1	Matrix	Rim	2210	25 690	7376	116754	26 436	90 013	15 361	1645	11747	3419	245	27
	1766-51.1	Matrix	Rim	2191	25 384	5074	119218	26 484	87 310	14 750	1475	10778	2544	186	29
	1766-52.1	Matrix	Core	1843	22 030	8097	117527	26 186	84383	14225	1611	10623	3507	270	23
	1766–53.1	Matrix	Core	2317	24 919	2067	119 799	26446	88796	15020	1573	11068	2692	178	24
Not included	1766–10.1	Matrix	Core	1604	18 254	9804	116944.4	25 3 1 7	81680	13386	1503	10029	3816	477	65
	1766–46.1	Matrix	Rim	3028	30 728	3122	121 206	26321	96471	16230	1650	11286	1811	92	15
	1766–54.1	Matrix		5354	77 559	4240	128767.4	30 228	95 230	15 589	1411	9251	2247	161	14

Table 5: Con	ıtinued										
Population	Spot name Grain	Grain	Spot	D	Тh	⊁	La	Pr	ŊĠ	Sm	Б
		1000	location (man)	(muu)	(muu)	(muu)	(maa) (maa)	(muu)		(muu)	

1	1	.!	1	:	É	*		ė	77.2		į	7	į	Ė	45
ropulation	Spot name	location	spor location	(mdd)	(mdd)	r (ppm)	(ppm)	(ppm)	(mdd)	(mdd)	(bpm)	(bpm)	(ppm)	(ppm)	(ppm)
Sample 17-64															
unclassified	1764-9.1	Matrix	Core	6481	41 996	18 504	121 186	30204	96411	17510	1170	16348	6597	877	107
	1764–20.1	Matrix	Core	3611	18 302	16354	117 341	27 046	88881	16034	1356	15210	9909	736	9/
	1764–35.1	Matrix	Core	4598	25 605	15 586	124 083	27 7 0 2	104 767	17691	1056	15931	5558	691	74
Monazite-I	1764–11.1	Matrix	Core	8665	53772	12 863	129 896	30 195	92473	16187	1055	13697	5102	633	89
	1764–16.1	Matrix	Core	3581	25 338	15 807	115 518	26 716	87 935	15948	1156	14750	5858	754	84
	1764–17.1	Matrix	Core	3562	22 282	16419	112262	26 802	88 693	16123	1065	14873	5912	758	83
	1764-19.1	Matrix	Core	3574	21 966	14 960	110085	27 560	89 490	16 134	1214	14905	5571	889	74
	1764-22.1	Matrix	Core	4201	25 973	17 150	116893	26 618	103 378	18 581	1245	16940	6305	764	81
	1764-23.1	Matrix	Core	4068	27 331	16 781	111652	27 253	94 178	17 312	1169	16207	6052	751	80
	1764–26.1	Matrix	Core	4537	35 129	17 068	115 565	28591	94642	17224	1216	15418	6052	764	98
	1764–28.1	Matrix	Core	5736	39 268	15 217	122 212	29171	93758	16968	1279	14974	2936	739	80
	1764–29.1	Matrix	Core	4919	37 869	15 524	116 690	28 806	889 96	17 105	1078	14867	5643	729	83
	1764–32.1	Matrix	Core	4038	26 359	14 738	111654	27 422	87 558	15616	1042	13595	5235	662	73
	1764–36.1	Matrix	Core	3911	21 025	14 263	112 557	26 156	89 562	15634	896	14258	5247	629	75
Monazite-II	1764-2.1	Matrix	Core	3977	25 862	15 833	117230	28 497	95 370	17 602	1366	15801	5874	692	84
	1764-3.1	Matrix	Core	3160	18073	15 766	114665	26 676	690 88	15 924	1327	14481	5954	9/9	9/
	1764 - 10.1	Matrix	Core	3979	20 991	13884	115419	26 982	89 184	15 901	1110	13929	5473	669	79
	1764–12.1	Matrix	Core	3300	21 039	15 619	114579	27 349	88 537	16052	1348	15097	5957	675	79
	1764-21.1	Matrix	Core	6265	42 397	13 755	117 105	27 884	103 075	17927	1008	14915	5245	664	73
	1764–24.1	Matrix	Core	3757	25 635	13 830	113773	26215	90323	16013	988	14367	5141	638	69
	1764-37.1	Matrix	Core	4448	27 453	15 628	112 809	27 572	90490	16175	1240	14515	5777	754	101
Monazite-III	1764-4.1	Matrix	Core	4136	25 380	11 505	113 685	26 123	86511	15228	1094	12628	4812	286	64
	1764-5.1	Matrix	Core	3560	20 695	12 892	111910	26 965	81 081	14563	1050	12756	5091	644	71
	1764-8.1	Matrix	Core	3461	24 189	10 782	114053	27 534	78 226	13823	1152	11095	4428	538	63
	1764-27.1	Matrix	Core	4264	30 698	11 161	111338	26 713	91 581	16 166	1441	12640	4906	581	65
	1764-30.1	Matrix	Core	3804	29 694	12 434	111650	28 325	89 297	16 327	1390	13629	4989	599	65
	1764-34.1	Matrix	Core	2743	15 480	13 457	115036	26033	82526	14552	1212	12768	4931	969	64
Not included	1764–14.1	Matrix	Core	6301	54 126	10 028	117 717	29461	122 930	22 192	1822	17274	6714	751	73
	1764–13.1	Matrix	Core	8565	87 272	10 364	112 089	26153	121 122	21492	1734	14247	5441	663	74
	1764–25.1	Matrix	Core	2060	32 936	13 270	113 374	26 608	92 249	16590	1399	13814	5571	689	9/
	1764–18.1	Matrix	Core	9859	29 926	12 357	117 061	26 426	103 091	17559	1494	12272	5187	730	97
	1764-7.1	Matrix	Core	3125	17 955	13 755	114724	27 088	80 522	14440	1104	13065	5361	9/9	80

Continues

Downloaded from https://academic.oup.com/petrology/article/63/8/egac068/6650310 by University of Iowa user on 24 August 2022

Manualle   Manualle						Conce	Concentrations <sup>b</sup>	Qs		Isotopic	Ratios (un	Isotopic Ratios (uncorrected) <sup>c</sup>		Isotopic ratios ( <sup>204</sup> Pb-correcte	Isotopic ratios ( <sup>204</sup> Pb-corrected) <sup>d</sup>	q		Date ( <sup>207</sup> Pb-co	Date ( <sup>207</sup> Pb-corrected) <sup>e</sup>
Disc.   Disc	Population	Analysis <sup>a</sup>	Grain	Spot	n	Th	Th/U	206Pb*	$f^{206}Pb_c$		% err	<sup>207</sup> Pb/	% err	238U/	% err	<sup>207</sup> Pb/	% err	206Pb/238	
766-711         Martin, Care         Care         2944         4170         14.5         16.5			location		(mdd) uc	(mdd)		(mdd)	(%)	<sup>206</sup> Pb	(1 s)	<sup>206</sup> Pb	(1 s)	<sup>206</sup> Pb	(1 s)	<sup>206</sup> Pb	(1 s)	(Ma)	(1 s)
1,046-011   Matrix   Care   2944   41770   145   145   162   0.0545   11   15818   15818   15   0.05595   12   146   15   15   15   15   15   15   15   1	Sample 17-66																		
Vice-131         Marrix         Rain         Sage         1244         1564         0.0564         0.7         1554         0.0         1754         15         0.0         15         0.0         15         0.0         15         0.0         15         0.0         15         0.0         15         0.0         15         0.0         15         0.0         15         0.0         15         0.0         0.0         15         0.0         15         0.0	Monazite-I	1766-01.1	Matrix	Core	2974	41770		162	0.26	15.755	1.2	0.0567	1.1	15.818	1.2	0.0535	2.2	396	2
1965-211         Matrix         Core         1974         18.78         10.6         18.87         0.6         18.87         10.6         19.89           19.66-171         Matrix         Core         19.84         10.6         18.47         0.6         18.78         0.6         18.78         0.6         18.78         0.6         18.78         0.6         18.78         0.6         18.78         0.6         18.78         0.6         18.78         0.6         18.78         0.6         18.78         0.6         18.78         0.6         18.78         0.6         18.78         0.6         0.654         1.0         0.658         0.6         18.78         0.6         0.658         0.6         18.78         0.6         0.658         0.6         18.78         0.6         0.658         0.6         18.78         0.6         0.658         0.6         18.78         0.6         0.658         0.6         18.78         0.6         0.658         0.6         18.78         0.6         0.658         0.6         18.78         0.6         0.658         0.6         18.78         0.6         0.658         0.6         18.78         0.6         0.658         0.6         18.78         0.6         0.658 </td <td></td> <td>1766-03.1</td> <td>Matrix</td> <td>Rim</td> <td>2256</td> <td>29 010</td> <td></td> <td>124</td> <td>0.24</td> <td>15.609</td> <td>9.0</td> <td>0.0566</td> <td>0.7</td> <td>15.654</td> <td>9.0</td> <td>0.0543</td> <td>1.1</td> <td>333</td> <td>2</td>		1766-03.1	Matrix	Rim	2256	29 010		124	0.24	15.609	9.0	0.0566	0.7	15.654	9.0	0.0543	1.1	333	2
1766-211   Matrix Core 2675 3120 128   15.2 167 0.25   0.055		1766–13.1	Matrix	Core	2774	36 069		150	0.31	15.798	9.0	0.0571	1.2	15.875	9.0	0.0532	1.6	394	7
		1766-17.1	Matrix	Core	3038	44653		167	0.19	15.631	0.5	0.0563	9.0	15.672	0.5	0.0542	1.0	339	7
		1766–18.1	Matrix	Core	2675	33120		148	0.62	15.443	9.0	0.0598	0.7	15.529	9.0	0.0554	1.4	402	2
Trick-2011   Matrix   Core   2012   438.20   156   157   157.95   0.6   0.05663   0.6   15.852   0.6   0.0544   0.7   0.0544   19   394   19.66-201   1.0   1.0   1.2		1766–19.1	Matrix	Core	3297	47 236		179	0.46	15.724	0.7	0.0584	9.0	15.781	0.7	0.0554	1.0	396	m
1766-211   Matrix   Core   2002   26812   115   110   021   15800   07   00056   0.6   15822   07   0.0045   10   394   1766-311   Matrix   Core   2002   26812   115   110   021   15800   07   0.0056   0.6   15802   07   0.0045   10   394   1766-311   18mt   Core   2416   2119   120   120   120   120   0.0057   0.6   15802   0.6   0.0044   11   28   399   1766-311   18mt   Core   2416   2119   120   120   120   120   0.0057   0.6   15802   0.6   0.0044   11   28   399   1766-311   18mt   Core   2416   2119   120   0.29   1572   120   0.0057   0.6   15802   0.6   0.0044   11   29   294   1766-311   18mt   Core   2416   2129   212   2120		1766-20.1	In grt	Core	1792	25077		97	0.21	15.759	9.0	0.0563	1.6	15.799	9.0	0.0543	1.9	396	7
Vice-311         Matrix         Core         3111         2209         1150         00570         008         15004         0.0544         18         399           Vice-3211         Matrix         Core         3131         42209         115         1509         0.05         1508         0.0544         11         399           Vice-3211         Matrix         Core         3151         42209         112         1509         0.05         1509         0.0544         11         399           Vice-3211         Matrix         Core         3151         45209         124         1509         0.0577         0.7         1589         0.0577         0.7         1589         0.0577         0.7         1589         0.0577         0.7         1589         0.0577         0.7         1589         0.0577         0.7         1589         0.0577         0.7         1589         0.0577         0.7         1589         0.0577         0.7         1589         0.0577         0.0577         0.0         1589         0.0577         0.0         1589         0.0577         0.0         1589         0.0         0.0577         0.0         1589         0.0         0.0577         0.0         1589		1766–21.1	Matrix	Core	2901	43820		157	0.27	15.806	0.7	0.0568	9.0	15.852	0.7	0.0545	1.0	394	m
Vice-S11         Matrix         Core         315         4.2563         13.9         12.0         13.0         15.0         15.0         15.0         10.0         15.0         15.0         10.0         15.0         15.0         10.0         15.0         10.0         15.0         10.0         15.0         10.0         15.0         10.0         10.0         15.0         10.0		1766-30.1	Matrix	Core	2052	26812		110	0.31	15.924	0.7	0.0570	8. 0	16.034	0.7	0.0514	J:8	391	ო (
Tribe-11 II Ingrit         Core         345         170         0.0554         1         352           1766-301 II Ingrit         Core         3416         51128 15.5         13         170         0.0554         0.05         15.882         10         0.0544         11         392           1766-421 II Matrix         Core         2426         30.90         12.4         13         0.05         12.6         0.057         0.0         15.889         10         0.0544         11         392           1766-421 II Matrix         Core         132         25.966         139         105         0.057         0.0         15.889         10         0.0544         11         392           1766-45.1 Matrix         Core         132         25.966         139         105         0.3         15.72         0         0.0556         0         0         0         15.889         0         0         0.0556         0		1766-31.1	Matrix	Core	3311	42 209		182	0.24	15.607	9.0	0.0567	9.0	15.708	9.0	0.0514	2.8	399	7
1766-421         Matrix         Care         415         5118         6         15846         10         534           1766-421         Matrix         Care         2524         5918         15.5         18         0.054         1.0         1584         1         0.0544         1         0.0544         1         0.0554         1         15.6         1         15.8         1         0.0544         1         0.0554         1         15.8         0         0.0544         1         0.0554         1         15.8         0         0.0544         1         0.0554         1         15.8         0         0.0544         1         0.0554         1         15.8         0         0.0544         1         0         0         0.0556         0 <t< td=""><td></td><td>1766–36.1</td><td>In grt</td><td>Core</td><td>3159</td><td>42563</td><td></td><td>170</td><td>0.32</td><td>15.909</td><td>9.0</td><td>0.0571</td><td>9.0</td><td>15.962</td><td>9.0</td><td>0.0544</td><td>1.1</td><td>392</td><td>7</td></t<>		1766–36.1	In grt	Core	3159	42563		170	0.32	15.909	9.0	0.0571	9.0	15.962	9.0	0.0544	1.1	392	7
1766-411   Matrix   Core   2224   30390   14.1   11.5   0.20   15.64   1.2   0.0575   1.5   1.5   1.5   1.5   0.0575   1.5   1.5   1.5   0.0575   1.5   1.5   1.5   0.0575   1.5   1.5   0.0575   1.5   1.5   0.0575		1766-39.1	Matrix	Core	3416	51138		185	0.28	15.823	1.0	0.0568	9.0	15.869	1.0	0.0545	1.0	394	4
1766-421   Matrix   Core   1932   25.995   141   115   0.20   15.654   12   0.0565   11   15.754   12   0.0561   18   398     1766-481   Matrix   Core   1932   25.995   143   156   0.24   15.22   0.6   0.0557   11   15.754   0.6   0.0557   15.89   0.6   0.0557   14   395     1766-481   Matrix   Core   1932   25.995   143   156   0.24   15.20   0.6   0.0565   0.7   15.89   0.6   0.0552   14   395     1766-0.01   Matrix   Core   1934   2.0744   116   99   0.76   15.889   0.6   0.0566   0.8   15.667   0.6   0.0552   14   395     1766-0.01   Matrix   Core   1934   17.912   19   94   0.24   15.889   0.6   0.0566   0.8   15.667   0.6   0.0552   14   395     1766-0.01   Matrix   Core   1934   17.02   1.0   0.24   15.28   0.9   0.0566   0.8   15.667   0.6   0.0552   14   395     1766-1.01   Matrix   Core   1934   1.102   9.9   0.2   16.138   0.9   0.0566   0.8   15.67   0.6   0.0553   1.8   396     1766-2.11   Matrix   Core   1.0   1.0   1.1   1.		1766-41.1	Matrix	Core	2524	30390		137	0.39	15.775	8.0	0.0577	0.7	15.840	8.0	0.0544	1.3	395	m
Trice-45,1 Matrix   Core   3188   53.285   13.9   105   0.56   15.742   0.6   0.0557   0.7   15.884   0.6   0.0518   1.8   396   1766-481   Matrix   Core   3188   53.285   1.3   1.5   1.5   0.2   0.0554   0.0   15.889   0.6   0.0558   1.4   395   1.5   395		1766–42.1	In grt	Core	2102	28672	14.1	115	0.20	15.654	1.2	0.0563	1.1	15.758	1.2	0.0509	2.3	398	2
1766-481         Matrix         Care         3188         3128         17.3         17.6         40         15.5         0.5         15.5         0.5         15.6         40         40           1766-492         Matrix         Care         2764         38284         14.3         15.0         0.34         15.89         0.5         0.5558         0.5         0.0581         1.1         395           1766-50.1         Matrix         Care         1849         2774         11.6         99         0.6         15.88         0.6         0.0587         0.6         15.88         0.6         0.0587         0.6         0.0587         0.6         0.0587         0.6         0.0587         0.6         0.0587         0.6         0.0587         0.6         0.0587         0.6         0.0587         0.6         0.0587         0.6         0.0587         0.6         0.0587         0.6         0.0587         0.6         0.0586         0.7         0.0587         0.8         0.0587         0.6         0.0586         0.7         0.0587         0.8         0.0587         0.8         0.0587         0.8         0.0587         0.8         0.0587         0.8         0.0587         0.8         0.0587		1766–45.1	Matrix	Core	1932	25936	13.9	105	0.36	15.742	9.0	0.0575	0.7	15.854	9.0	0.0518	1.8	396	2
1766-49.2         Matrix         Core         2764         188.24         14.3         150         0.4         0.0665         0.0         15.839         0.6         0.0530         14         398           1766-20.1         Matrix         Core         475.2         41.3         15.2         0.4         15.528         0.9         0.0565         0.6         15.839         0.9         0.0552         18         398           1766-07.1         Matrix         Core         41849         2.0         15.828         0.9         0.0566         0.7         15.829         0.9         0.0552         1.8         396           1766-07.1         Matrix         Core         1784         15.781         1.6         0.0566         0.7         16.208         0.9         0.0569         0.7         0.0569         0.9         0.0569         0.7         0.0569         0.9         0.0569         0.9         0.0569         0.7         0.0569         0.9         0.0569         0.9         0.0569         0.9         0.0569         0.9         0.0569         0.9         0.0569         0.9         0.0569         0.9         0.0569         0.9         0.0569         0.9         0.0569         0.9 <td< td=""><td></td><td>1766-48.1</td><td>Matrix</td><td>Core</td><td>3188</td><td>53 285</td><td>17.3</td><td>176</td><td>0.33</td><td>15.527</td><td>0.5</td><td>0.0574</td><td>9.0</td><td>15.578</td><td>0.5</td><td>0.0548</td><td>1.0</td><td>401</td><td>2</td></td<>		1766-48.1	Matrix	Core	3188	53 285	17.3	176	0.33	15.527	0.5	0.0574	9.0	15.578	0.5	0.0548	1.0	401	2
Toff-Sol Matrix         Core         1892         41573         414         167         044         1858         04         0.0552         0.0551         1.1         398           1766-02.1         Matrix         Core         1849         1576-7         1588         0.9         0.0559         0.6         0.0552         1.8         391           1766-02.1         Matrix         Core         1849         15878         8.2         1.6128         0.7         0.0569         0.7         16286         0.0         0.0541         1.7         384           1766-0.1.1         Matrix         Core         1787         1.1         1.2         9.9         0.0         0.0564         0.7         16.39         0.6         0.0554         1.7         384           1766-0.1.1         Matrix         Core         1.481         1.6146         1.1         0.2         16.11         0.0         0.0567         0.8         16.14         0.0         0.0559         1.7         384           1766-2.1         Matrix         Rim         2.9         1.4         1.613         0.9         0.0567         0.8         16.148         0.9         0.0559         1.8         384		1766–49.2	Matrix	Core	2764	38 284	14.3	150	0.24	15.790	9.0	0.0565	0.7	15.859	9.0	0.0530	1.4	395	2
1766-0.1   Matrix   Core   1849   20714   116   99   0.76   15.889   0.6   0.6666   0.8   15.967   0.6   0.0552   18   391     1766-0.1   Matrix   Core   1787   17152   2.9   94   0.29   16.222   0.5   0.0564   0.7   16.238   0.7   0.0543   1.7   386     1766-0.1   Matrix   Rim   2381   26.939   11.7   125   0.29   16.212   0.5   0.0564   0.7   16.239   0.5   0.0543   1.7   384     1766-1.1   Matrix   Rim   242   20.723   8.8   1.28   0.29   16.124   0.6   0.0564   0.7   16.337   0.9   0.0537   1.2   384     1766-2.1   Matrix   Core   2069   24.83   1.2   1.2   1.2   2.9   16.114   0.6   0.0567   0.8   16.148   0.6   0.0557   0.8   16.148   0.6   0.0547   0.8     1766-2.1   Matrix   Core   2069   24.83   1.2		1766-50.1	Matrix	Core	3052	41573	14.1	167	0.43	15.628	6.0	0.0582	9.0	15.687	6.0	0.0551	1.1	398	က
1766-07.1         Matrix         Core         1974         15587         8.2         105         6.21         6.656         0.7         6.626         0.7         6.626         0.7         6.626         0.7         6.626         0.7         6.626         0.7         6.627         1.7         384           1766-08.1         Matrix         Rim         2.482         1.787         1.7         1.25         0.29         1.2         16.283         0.5         0.656         0.0584         1.4         16.304         0.6         0.0584         1.4         16.309         0.6         0.0584         1.7         1.2         1.2         0.2         16.283         0.6         0.0584         1.4         16.309         0.6         0.0584         1.4         16.309         0.6         0.0584         1.4         16.309         0.6         0.0584         1.4         16.309         0.6         0.0584         1.4         16.309         0.6         0.0584         1.4         16.309         0.6         0.0584         1.4         16.309         0.6         0.0584         1.4         16.309         0.6         0.0584         1.4         16.309         0.6         0.0584         1.4         16.309         0.6	Monazite-II	1766-02.1	Matrix	Core	1849	20714	11.6	66	92.0	15.859	9.0	9090'0	8.0	15.967	9.0	0.0552	1.8	391	2
1766-08.1         Matrix         Core         1787         17102         99         4         0.29         16252         0.5         0.054         1         16304         0.6         0.0541         1.7         384           1766-11.1         Matrix         Sim         2693         1,25         0.26         16283         0.9         0.0584         1.4         16309         0.0583         1.2         383           1766-11.1         Matrix         Core         1422         20.23         8.8         1.25         0.29         16111         0.6         0.0567         0.6         0.0573         1.2         384           1766-21.1         Matrix         Core         1481         1614         1.1         0.29         16111         0.6         0.057         0.8         16148         0.6         0.057         0.8         1619         0.057         0.057         0.8         1619         0.056         0.057         0.8         1619         0.056         0.057         0.8         1619         0.056         0.057         0.8         1619         0.056         0.057         0.8         1619         0.0         0.056         0.8         1619         0.0         0.057         0.8		1766-07.1	Matrix	Core	1974	15587	8.2	105	0.21	16.173	0.7	0.0560	0.7	16.208	0.7	0.0543	1.0	386	ო
Trice-111   Matrix   Rim   2381   26939   11.7   125   0.26   16.283   0.9   0.0564   0.7   16.337   0.9   0.0538   1.2   383   1.7   1.7   1.7   1.5   0.2   1.5   0.25   0.0584   1.4   16.309   0.6   0.0539   1.2   384   1.7   1.7   1.5   1.5   1.5   0.5   0.0559   0.6   0.0559   0.6   0.0539   0.6   0.0539   1.2   384   1.7   1.7   1.5   1.5   1.5   1.5   0.0   0.0567   0.8   16.14   0.6   0.0559   0.6   0.0539   1.5   384   1.7   1.7   1.2   1.5   1.5   1.5   1.5   0.5   0.0550   0.8   16.14   0.6   0.0559   1.5   384   1.7   1.7   1.2   1.5   1.5   1.5   0.5   0.0550   0.8   16.15   0.6   0.0552   1.5   384   1.7   1.7   1.2   1.5   1.5   1.5   0.5   0.0565   0.8   16.15   0.8   0.0565   0.8   16.15   0.8   0.0565   0.8   16.15   0.8   0.0565   0.8   1.5   0.0552   1.5   384   1.7   1.7   1.2   0.4   1.5   1.2   0.5   0.0559   0.7   1.5   1.5   0.5   0.0542   1.5   384   1.7   1.7   1.2   1.2   0.4   1.5   1.4   0.5   0.0559   0.7   1.5   1.5   0.5   0.0542   1.4   381   1.7   1.7   1.2   0.4   1.5   1.5   0.5   0.0559   0.7   1.5   1.5   0.5   0.0542   1.4   381   1.7   1.5   0.5   0.0559   0.7   1.5   0.5   0.0559   0.7   1.5   0.5   0.0559   0.7   0		1766-08.1	Matrix	Core	1787	17102	6.6	94	0.29	16.252	0.5	0.0567	1.4	16.304	9.0	0.0541	1.7	384	2
1766-14.1         Matrix         Rim         2422         20723         8.8         128         0.51         16149         0.6         0.0584         14         16309         0.6         0.0527         2.2         384           1766-22.1         Matrix         Core         1481         16146         1.13         79         0.29         16.11         0.6         0.0556         0.8         16.148         0.6         0.0529         1.2         387           1766-22.1         Matrix         Core         2490         1.24         1.14         0.22         16.03         0.6         0.0576         0.8         16.14         0.6         0.0529         1.6         387           1766-28.1         Matrix         Core         2490         1.19         1.2         1.6         0.0         0.056         0.8         16.17         0.6         0.057         0.8         16.27         0.6         0.057         0.8         16.27         0.6         0.055         0.8         16.27         0.8         16.27         0.6         0.055         0.8         16.27         0.6         0.054         0.8         16.27         0.6         0.054         1.9         1.9         1.2         1.1 <td></td> <td>1766-11.1</td> <td>Matrix</td> <td>Rim</td> <td>2381</td> <td>26939</td> <td>11.7</td> <td>125</td> <td>0.26</td> <td>16.283</td> <td>6.0</td> <td>0.0564</td> <td>0.7</td> <td>16.337</td> <td>6.0</td> <td>0.0538</td> <td>1.2</td> <td>383</td> <td>ო</td>		1766-11.1	Matrix	Rim	2381	26939	11.7	125	0.26	16.283	6.0	0.0564	0.7	16.337	6.0	0.0538	1.2	383	ო
1766-22.1         Matrix         Core         1481         1644         11.3         79         0.29         16.111         0.6         0.0567         0.8         16.148         0.6         0.0549         1.2         387           1766-23.1         Matrix         Core         2069         24.837         12.4         110         0.32         16.039         0.6         0.0570         0.8         16.174         0.6         0.0530         1.6         387           1766-23.1         Matrix         Core         2137         26.60         1.19         1.2         16.039         0.6         0.0560         0.8         16.179         0.6         0.0567         0.8         16.179         0.6         0.0579         0.8         16.179         0.6         0.0567         0.8         16.179         0.6         0.0579         0.8         16.279         0.6         0.0579         0.8         16.279         0.6         0.0579         0.8         16.279         0.6         0.0579         0.8         16.279         0.6         0.0579         0.8         16.279         0.6         0.0579         0.8         16.279         0.6         0.0579         0.8         16.279         0.8         16.279 <t< td=""><td></td><td>1766–14.1</td><td>Matrix</td><td>Rim</td><td>2422</td><td>20723</td><td>8.8</td><td>128</td><td>0.51</td><td>16.194</td><td>9.0</td><td>0.0584</td><td>1.4</td><td>16.309</td><td>9.0</td><td>0.0527</td><td>2.2</td><td>384</td><td>2</td></t<>		1766–14.1	Matrix	Rim	2422	20723	8.8	128	0.51	16.194	9.0	0.0584	1.4	16.309	9.0	0.0527	2.2	384	2
1766-23.1   Matrix   Core   2069   24.837   12.4   110   0.32   16.093   0.6   0.0570   0.8   16.174   0.6   0.0530   1.6   387   1766-25.1   Matrix   Core   2122   22.430   10.6   114   0.23   16.428   0.6   0.0564   0.8   16.571   0.6   0.0525   1.6   380   1766-27.1   Matrix   Core   213.7   26609   11.9   123   0.25   16.190   0.6   0.0564   0.8   16.223   0.6   0.0552   1.6   385   1766-38.1   Matrix   Core   2415   27.439   11.7   128   0.44   16.114   0.5   0.0579   1.4   16.172   0.6   0.0554   1.3   386   1766-37.1   Matrix   Core   2415   27.439   1.7   1.28   0.44   16.114   0.5   0.0579   0.7   16.413   0.6   0.0554   1.4   381   1766-40.1   Matrix   Rim   1989   21518   1.2   0.4   16.134   0.5   0.0579   0.7   16.413   0.6   0.0530   1.7   388   1766-40.1   Matrix   Rim   2160   22.819   1.9   115   0.4   16.138   1.2   0.0584   0.9   0.0579   1.4   16.134   0.6   0.0530   1.4   381   1766-40.1   Matrix   Rim   2160   22.819   1.0   115   0.4   16.234   0.6   0.0579   0.9   16.234   0.9   0.0530   1.4   382   1.4   382   1.4   382   1.4   382   1.4   383   383   383   383   383   383   383   383   383   383   383   383   383   383   383   383   383		1766-22.1	Matrix	Core	1481	16 146	11.3	79	0.29	16.111	9.0	0.0567	8.0	16.148	9.0	0.0549	1.2	387	2
1766-26.1         Matrix         Core         2192         22430         10.6         114         0.23         16.428         0.6         0.0561         0.8         16.501         0.6         0.0525         1.6         380           1766-26.1         Matrix         Core         2317         26609         1.19         123         0.52         16.074         0.8         0.0586         0.8         16.157         0.8         0.0554         1.5         387           1766-27.1         Matrix         Core         1824         19.14         1.2         16.19         0.6         0.0564         0.8         16.172         0.6         0.0525         1.6         387           1766-24.1         Matrix         Core         2415         2.743         1.1         128         0.4         16.114         0.5         0.0564         0.8         16.273         0.6         0.0554         1.4         387           1766-37.1         Matrix         Rim         1989         21518         1.1         104         0.45         16.34         0.6         0.0579         0.7         16.413         0.6         0.0579         0.7         16.419         0.6         0.0579         0.7         16.419 </td <td></td> <td>1766–23.1</td> <td>Matrix</td> <td>Core</td> <td>2069</td> <td>24 837</td> <td>12.4</td> <td>110</td> <td>0.32</td> <td>16.093</td> <td>9.0</td> <td>0.0570</td> <td>0.8</td> <td>16.174</td> <td>9.0</td> <td>0.0530</td> <td>1.6</td> <td>387</td> <td>2</td>		1766–23.1	Matrix	Core	2069	24 837	12.4	110	0.32	16.093	9.0	0.0570	0.8	16.174	9.0	0.0530	1.6	387	2
1766-27.1         Matrix         Core         2317         26609         11.9         123         0.52         16.074         0.8         0.0586         0.8         16.157         0.8         0.0545         1.5         387           1766-28.1         Matrix         Core         1824         19134         10.8         96         0.29         16.190         0.6         0.0554         0.8         16.275         0.6         0.0525         1.6         385           1766-34.1         Matrix         Core         1815         18.8         96         0.25         16.19         0.6         0.0549         0.8         16.275         0.6         0.0525         1.9         385           1766-34.1         Matrix         Core         2415         27439         1.7         128         0.4         16.14         0.5         0.0579         0.7         16.413         0.6         0.0579         0.7         16.413         0.6         0.0579         0.7         16.413         0.8         0.0579         0.7         16.419         0.8         0.0579         0.7         0.0589         0.0530         0.7         0.0589         0.0         0.0592         0.7         0.0589         0.7         0.0589		1766–26.1	Matrix	Core	2192	22430	10.6	114	0.23	16.428	9.0	0.0561	8.0	16.501	9.0	0.0525	1.6	380	2
1766–28.1         Matrix         Core         1824         19134         10.8         96         0.29         16.190         0.6         0.0567         0.8         16.275         0.6         0.0525         1.6         385           1766–28.1         Matrix         Core         1815         1808         10.3         96         0.25         16.179         0.6         0.0564         0.8         16.223         0.6         0.0542         1.3         386           1766–35.1         Matrix         Core         1789         11.7         128         0.44         16.14         0.5         0.0579         0.7         16.413         0.6         0.0554         1.8         386           1766–37.1         Matrix         Rim         1989         21518         11.2         104         0.45         1.6         0.0579         0.7         16.499         0.6         0.0579         1.4         381           1766–37.1         Matrix         Rim         2100         22819         1.09         1.5         0.6         0.0579         0.9         0.0530         1.7         382           1766–37.1         Matrix         Rim         2191         2.2         1.2         1.2		1766-27.1	Matrix	Core	2317	26 609	11.9	123	0.52	16.074	8.0	0.0586	0.8	16.157	8.0	0.0545	1.5	387	m
1766-34.1 Matrix Core 1815 18085 10.3 96 0.25 16.179 0.6 0.0564 0.8 16.223 0.6 0.0542 1.3 386 1766-35.1 Matrix Core 2415 27439 11.7 128 0.44 16.114 0.5 0.0579 1.4 16.172 0.6 0.0551 1.8 386 1766-37.1 Matrix Rim 1989 21518 11.2 104 0.45 16.344 0.6 0.0579 0.7 16.413 0.6 0.0545 1.4 381 1766-40.1 Matrix Rim 2100 22819 10.9 115 0.41 16.054 0.6 0.0577 0.8 16.49 0.9 0.0537 1.6 382 1766-49.1 Matrix Rim 2101 25.84 12.0 117 0.80 16.138 1.2 0.0608 1.9 16.251 1.2 0.0552 2.7 385 1766-51.1 Matrix Rim 2191 25.384 12.0 115 0.53 16.252 0.7 0.0586 0.7 16.354 0.6 0.0535 1.9 383 1766-51.1 Matrix Core 1843 22.030 12.4 97 0.59 16.235 0.6 0.0591 0.9 16.347 0.6 0.0535 1.9 383 1766-51.1 Matrix Core 16.04 18.254 11.8 86 1.69 1.5721 1.2 0.0682 1.8 15.997 1.2 0.0542 3.7 391 1766-64.1 Matrix Rim 3028 30.28 10.5 16.6 1.60 15.721 1.2 0.06746 5.7 14.713 0.9 0.0556 3.0 399 1766-54.1 Matrix Rim 3028 30.28 10.5 16.4 3.8 14.316 0.6 0.0746 5.7 14.713 0.9 0.0557 13.0 425		1766–28.1	Matrix	Core	1824	19134	10.8	96	0.29	16.190	9.0	0.0567	0.8	16.275	9.0	0.0525	1.6	382	7
1766-35.1         Matrix         Core         2415         27439         11.7         128         0.44         16.114         0.5         0.0579         1.4         16.172         0.6         0.0551         1.8         386           1766-35.1         Matrix         Rim         1989         21518         11.2         104         0.45         16.344         0.6         0.0579         0.7         16.413         0.6         0.0557         1.4         381           1766-40.1         Matrix         Rim         2160         22.819         10.9         115         0.41         16.054         0.6         0.0577         0.8         16.499         0.9         0.0537         1.6         382           1766-40.1         Matrix         Rim         2210         25.690         12.0         117         0.80         16.252         0.7         0.0586         0.7         16.354         0.6         0.0577         0.8         16.257         1.7         382           1766-5.1         Matrix         Rim         2210         25.890         12.0         117         0.80         16.252         0.7         0.0586         0.7         0.0556         1.9         0.0557         0.8         16.34		1766–34.1	Matrix	Core	1815	18085	10.3	96	0.25	16.179	9.0	0.0564	8.0	16.223	9.0	0.0542	1.3	386	7
1766–37.1         Matrix         Rim         1989         21518         11.2         104         0.45         16.344         0.6         0.0579         0.7         16.413         0.6         0.0545         1.4         381           1766–40.1         Matrix         Core         1709         19776         12.0         90         0.50         16.314         0.9         0.0583         0.8         16.499         0.9         0.0537         16         382           1766–40.1         Matrix         Rim         210         22.819         10.9         115         0.41         16.054         0.6         0.0577         0.8         16.149         0.6         0.0530         1.7         382           1766–49.1         Matrix         Rim         2210         25.890         12.0         117         0.80         16.252         0.7         0.0586         0.7         16.354         0.9         0.0586         0.7         0.0586         0.7         0.0536         1.6         383         1.6         383         1.6         383         1.6         383         1.6         383         1.6         384         1.6         1.6         1.8         1.6         0.0531         1.8         1.6 </td <td></td> <td>1766–35.1</td> <td>Matrix</td> <td>Core</td> <td>2415</td> <td>27439</td> <td>11.7</td> <td>128</td> <td>0.44</td> <td>16.114</td> <td>0.5</td> <td>0.0579</td> <td>1.4</td> <td>16.172</td> <td>9.0</td> <td>0.0551</td> <td>1.8</td> <td>386</td> <td>2</td>		1766–35.1	Matrix	Core	2415	27439	11.7	128	0.44	16.114	0.5	0.0579	1.4	16.172	9.0	0.0551	1.8	386	2
1766-40.1 Matrix Core 1709 19776 12.0 90 0.50 16.314 0.9 0.0583 0.8 16.409 0.9 0.0537 1.6 382 1766-46.1 Matrix Rim 2160 22819 10.9 115 0.41 16.054 0.6 0.0577 0.8 16.149 0.6 0.0530 1.7 388 1766-49.1 Matrix Rim 210 25.80 12.0 117 0.80 16.138 1.2 0.0608 1.9 16.251 1.2 0.0552 2.7 385 1766-49.1 Matrix Core 1843 22.030 12.4 97 0.59 16.235 0.6 0.0591 0.9 16.347 0.6 0.0536 1.9 383 1766-51.1 Matrix Core 2317 24.919 11.1 121 0.92 16.294 0.8 0.0617 0.8 16.500 0.8 0.0516 2.3 381 1766-40.1 Matrix Rim 3028 30.728 10.5 16.0 1.60 15.70 1.8 16.20 0.8 0.0676 1.6 1.6 15.619 0.8 0.0556 3.0 399 1766-54.1 Matrix Rim 3028 30.728 10.5 16.0 1.60 15.40 0.8 0.0676 1.6 1.6 15.619 0.8 0.0556 3.0 399 1766-54.1 Matrix Rim 3028 30.728 10.5 16.0 1.60 15.40 0.8 0.00746 5.7 14.713 0.9 0.0557 13.0 425		1766-37.1	Matrix	Rim	1989	21518	11.2	104	0.45	16.344	9.0	0.0579	0.7	16.413	9.0	0.0545	1.4	381	2
1766-46.2 Matrix Rim 2160 22819 10.9 115 0.41 16.054 0.6 0.0577 0.8 16.149 0.6 0.0530 1.7 388 1766-49.1 Matrix Rim 2210 25690 12.0 117 0.80 16.138 1.2 0.0608 1.9 16.251 1.2 0.0552 2.7 385 1766-49.1 Matrix Core 1843 22.030 12.4 97 0.59 16.235 0.6 0.0591 0.9 16.347 0.6 0.0536 1.9 383 1766-51.1 Matrix Core 2317 24.919 11.1 121 0.92 16.294 0.8 0.0617 0.8 16.500 0.8 0.0516 2.3 381 1766-40.1 Matrix Rim 3028 30.728 10.5 16.0 15.0 15.20 1.8 16.20 0.8 0.0656 3.0 3.0 3.9 1766-40.1 Matrix Rim 3028 30.728 10.5 16.0 15.0 18.4 2.3 14.316 0.6 0.0746 5.7 14.713 0.9 0.0557 13.0 4.25		1766-40.1	Matrix	Core	1709	19776		90	0.50	16.314	6.0	0.0583	0.8	16.409	6.0	0.0537	1.6	382	m
1766-49.1 Matrix Rim 2210 25690 12.0 17 0.80 16.138 1.2 0.0608 1.9 16.251 1.2 0.0552 2.7 385 1766-51.1 Matrix Core 1843 22030 12.4 97 0.59 16.235 0.6 0.0591 0.9 16.347 0.6 0.0535 1.9 383 1766-52.1 Matrix Core 2317 24919 11.1 121 0.92 16.294 0.8 0.0617 0.8 16.500 0.8 0.0516 2.3 381 1766-40.1 Matrix Core 1604 18.254 11.8 86 1.69 15.721 1.2 0.0682 1.8 15.997 1.2 0.0566 3.0 399 1766-40.1 Matrix Rim 3028 30.728 10.5 16.0 15.406 0.8 0.00746 5.7 14.713 0.9 0.0557 13.0 425		1766-46.2	Matrix	Rim	2160	22819	10.9	115	0.41	16.054	9.0	0.0577	8.0	16.149	9.0	0.0530	1.7	388	2
1766-51.1 Matrix Rim 2191 25384 12.0 115 0.53 16.252 0.7 0.0586 0.7 16.354 0.7 0.0536 1.6 <b>383</b> 1766-52.1 Matrix Core 1843 22030 12.4 97 0.59 16.235 0.6 0.0591 0.9 16.347 0.6 0.0535 1.9 <b>383</b> 1766-53.1 Matrix Core 2317 24919 11.1 121 0.92 16.294 0.8 0.0617 0.8 16.500 0.8 0.0516 2.3 <b>381</b> 1766-40.1 Matrix Rim 3028 30.728 10.5 160 1.60 15.406 0.8 0.0676 1.6 15.619 0.8 0.0566 3.0 399 1766-54.1 Matrix Rim 528 7.559 15.0 314 2.38 14.316 0.6 0.0746 5.7 14.713 0.9 0.0527 13.0 425		1766-49.1	Matrix	Rim	2210	25 690		117	0.80	16.138	1.2	0.0608	1.9	16.251	1.2	0.0552	2.7	382	2
1766–52.1 Matrix Core 1843 22030 12.4 97 0.59 16.235 0.6 0.05591 0.9 16.347 0.6 0.0535 1.9 <b>383</b> 1766–53.1 Matrix Core 2317 24919 11.1 121 0.92 16.294 0.8 0.0617 0.8 16.500 0.8 0.0516 2.3 <b>381</b> 1766–10.1 Matrix Core 1604 18.254 11.8 86 1.69 15.721 1.2 0.0682 1.8 15.997 1.2 0.0542 3.7 391 1766–46.1 Matrix Rim 3028 30.728 10.5 166 1.60 15.406 0.8 0.0676 1.6 15.619 0.8 0.0566 3.0 399 1766–54.1 Matrix Rim 5384 77559 15.0 314 2.38 14.316 0.6 0.0746 5.7 14.713 0.9 0.0527 13.0 425		1766-51.1	Matrix	Rim	2191	25384	12.0	115	0.53	16.252	0.7	0.0586	0.7	16.354	0.7	0.0536	1.6	383	ო
1766–53.1 Matrix Core 2317 24919 11.1 121 0.92 16.294 0.8 0.0617 0.8 16.500 0.8 0.0516 2.3 <b>381</b> 1766–10.1 Matrix Core 1604 18.254 11.8 86 1.69 15.721 1.2 0.0682 1.8 15.997 1.2 0.0542 3.7 391 1766–46.1 Matrix Rim 3028 30.728 10.5 166 1.60 15.406 0.8 0.0676 1.6 15.619 0.8 0.0566 3.0 399 1766–54.1 Matrix Rim 5354 77559 15.0 314 2.38 14.316 0.6 0.0746 5.7 14.713 0.9 0.0527 13.0 425		1766-52.1	Matrix	Core	1843	22030	12.4	26	0.59	16.235	9.0	0.0591	6.0	16.347	9.0	0.0535	1.9	383	2
1766–10.1 Matrix Core 1604 18254 11.8 86 1.69 15.721 1.2 0.0682 1.8 15.997 1.2 0.0542 3.7 391 1766–46.1 Matrix Rim 3028 30728 10.5 166 1.60 15.406 0.8 0.0676 1.6 15.619 0.8 0.0566 3.0 399 1766–54.1 Matrix 5354 77559 15.0 314 2.38 14.316 0.6 0.0746 5.7 14.713 0.9 0.0527 13.0 425		1766-53.1	Matrix	Core	2317	24919	11.1	121	0.92	16.294	8.0	0.0617	8.0	16.500	8.0	0.0516	2.3	381	က
Matrix         Rim         3028         30728         10.5         16         1.6         15.406         0.8         0.0676         1.6         1.6         1.5         1.9         0.8         0.0566         3.0         399           Matrix         5354         77 559         15.0         314         2.38         14.316         0.6         0.0746         5.7         14.713         0.9         0.0527         13.0         425	Not included	1766-10.1	Matrix	Core	1604	18 254	11.8	98	1.69	15.721	1.2	0.0682	1.8	15.997	1.2	0.0542	3.7	391	2
Matrix 5354 77559 15.0 314 2.38 14.316 0.6 0.0746 5.7 14.713 0.9 0.0527 13.0 425		1766-46.1	Matrix	Rim	3028	30 728	10.5	166	1.60	15.406	8.0	0.0676	1.6	15.619	8.0	0.0566	3.0	399	m
		1766-54.1	Matrix		5354	77 559	15.0	314	2.38	14.316	9.0	0.0746	5.7	14.713	6.0	0.0527	13.0	425	cc

Table 6: Monazite U-Pb

Downloaded from https://academic.oup.com/petrology/article/63/8/egac068/6650310 by University of lowa user on 24 August 2022

Table 6: Continued

ide :	יווומכמ																	
					Concen	Concentrations <sup>b</sup>		1	Isotopic	Ratios (und	Isotopic Ratios (uncorrected) °	I	Isotopic ratios ( <sup>204</sup> Pb-correcte	Isotopic ratios ( <sup>204</sup> Pb-corrected) <sup>d</sup>		ı	Date ( <sup>207</sup> Pb-cc	Date ( <sup>207</sup> Pb-corrected) <sup>e</sup>
Population	Analysis <sup>a</sup>	Grain location	Spot location	Spot U location (ppm)	Th (ppm)	Th/U	<sup>206</sup> Pb* (ppm)	f <sup>206</sup> Pb <sub>c</sub> (%)	238U/ 206Pb	% err (1 s)	<sup>207</sup> Pb/ <sup>206</sup> Pb	% err (1 s)	238U/ 206Pb	% err (1 s)	<sup>207</sup> Pb/ <sup>206</sup> Pb	% err (1 s)	<sup>206</sup> Pb/ <sup>238</sup> U (Ma)	U err abs (1 s)
Sample 17-64																		
unclassified	1764-9.1	Matrix	Core	6481	41996	6.7	368	90.0	15.121	0.5	0.0555	9.0	15.152	0.5	0.0539	0.8	413	2
	1764-20.1	Matrix	Core	4598	25 605	5.2	201	0.19	15.302	0.5	0.0564	0.5	15.415	1.7	0.0554	5.2	407	2
	1764-35.1	Matrix	Core	3611	18302	5.8	258	0.41	15.363	1.7	0.0581	4.3	15.357	0.5	0.0535	6.0	405	7
Monazite-I	1764-11.1	Matrix	Core	8665	53772	6.4	474	0.10	15.678	6.0	0.0555	0.7	15.709	6.0	0.0538	1.0	398	4
	1764-16.1	Matrix	Core	4919	37869	7.3	194	0.27	15.663	9.0	0.0569	9.0	15.942	0.5	0.0520	1.2	398	2
	1764-17.1	Matrix	Core	4201	25973	6.5	193	0.03	15.803	0.7	0.0549	0.5	15.851	9.0	0.0530	8.0	395	က
	1764-19.1	Matrix	Core	3562	22 282	6.4	194	0.07	15.809	9.0	0.0552	0.5	15.895	9.0	0.0528	1.5	395	2
	1764-22.1	Matrix	Core	3911	21025	6.4	228	60.0	15.845	0.7	0.0553	0.5	15.829	0.7	0.0536	0.7	394	က
	1764-23.1	Matrix	Core	3574	21 966	6.9	220	0.18	15.832	9.0	0.0560	1.1	15.898	9.0	0.0530	8.0	394	က
	1764-26.1	Matrix	Core	4068	27331	8.0	244	0.01	15.866	9.0	0.0547	0.5	16.002	0.5	0.0530	1.5	394	2
	1764-28.1	Matrix	Core	3581	25338	7.1	309	0.25	15.851	0.5	0.0566	0.5	15.944	0.7	0.0541	2.4	393	2
	1764-29.1	Matrix	Core	4038	26359	8.0	269	0.01	15.893	1.0	0.0547	1.3	15.747	9.0	0.0526	1.4	393	4
	1764-32.1	Matrix	Core	5736	39268	6.7	218	0.35	15.879	0.7	0.0574	2.0	15.929	1.0	0.0528	1.5	392	ო
	1764-36.1	Matrix	Core	4537	35129	5.6	212	0.27	15.929	0.5	0.0567	1.0	15.876	0.7	0.0537	0.7	391	2
Monazite-II	1764-2.1	Matrix	Core	3160		2.9	213	0.26	15.973	9.0	0.0566	9.0	16.051	0.5	0.0545	1.8	390	2
	1764-3.1	Matrix	Core	3757	25 635	5.9	170	90.0	16.020	0.7	0.0549	0.5	16.014	9.0	0.0545	6.0	390	ო
	1764-10.1	Matrix	Core	3977	25862	5.5	212	0.45	15.981	0.5	0.0581	1.4	16.148	8.0	0.0543	1.4	390	2
	1764-12.1	Matrix	Core	3300	21039	9.9	176	0.17	16.082	0.7	0.0558	9.0	16.118	0.7	0.0540	6.0	388	ო
	1764-21.1	Matrix	Core	6265	42397	7.0	334	0.08	16.121	1.2	0.0551	9.0	16.153	1.2	0.0534	8.0	388	4
	1764-24.1	Matrix	Core	3979	20991	7.0	201	0.23	16.107	0.7	0.0563	1.2	16.056	0.7	0.0532	0.7	387	ო
	1764-37.1	Matrix	Core	4448		6.4	235	0.26	16.225	9.0	0.0564	9.0	16.281	9.0	0.0536	1.0	385	7
Monazite-III	1764-4.1	Matrix	Core	4136	25380	6.3	215	0.52	16.446	9.0	0.0584	0.7	16.532	9.0	0.0542	1.3	379	7
	1764-5.1	Matrix	Core	3560		0.9	184	0.15	16.591	0.7	0.0554	9.0	16.632	0.7	0.0534	1.0	377	ო
	1764-8.1	Matrix	Core	2743	15 480	7.2	176	0.58	16.645	1.1	0.0588	1.4	16.904	6.0	0.0541	1.5	374	4
	1764-27.1	Matrix	Core	3804	29694	7.4	212	0.13	16.763	2.2	0.0551	0.7	17.227	1.0	0.0547	5.9	373	∞
	1764-30.1	Matrix	Core	3461	24189	8.1	195	0.77	16.776	6.0	0.0602	9.0	16.827	2.2	0.0521	1.2	370	ო
	1764-34.1	Matrix	Core	4264	30698	5.8	141	0.84	17.101	1.0	9090'0	3.2	16.733	1.1	0.0546	1.8	363	4
Not included	1764-7.1	Matrix	Core	2060	32936	5.9	170	1.97	16.526	1.1	0.0699	7.7	15.821	0.7	0.0527	2.8	372	2
	1764-13.1	Matrix	Core	8565	87272	10.5	415	12.33	15.542	1.7	0.1530	5.7	17.040	2.0	0.0849	14.9	354	7
	1764-14.1	Matrix	Core	3125	17955	8.9	326	2.53	15.384	9.0	0.0751	1.0	15.197	1.9	0.1215	6.4	396	m
	1764–18.1	Matrix	Core	9859	29 926	4.7	328	2.28	16.832	1.0	0.0722	2.8	17.197	1.0	0.0551	5.4	364	4
	1764–25.1	Matrix	Core	6301	54126	6.7	258	10.97	14.762	1.8	0.1427	4.2	16.839	1.3	0.0549	12.6	378	7

Note: All analyses were performed on the SHRIMP-RG ion microprobe at the United States Geological Survey-Stanford Microanalytical Center at Stanford University. The analytical routine followed Barth & Wooden (2006, 2010). Data reduction utilized the Squid 2.51 program of Ludwig (2009). Analyses in bold were used in age calculation. Ppb\* denotes radiogenic Pb; Pbc denotes common Pb; Pbc denotes compositions were based on replicate analyses of monazite reference material 44069 (424.9 ± 0.5 Ma; Aleinikoff et al., 2006, 2012) Reported ratios are not corrected for common Pb. Initial common Pb isotopic composition approximated from Stacey & Kramers (1975). Uncertainties reported as 1 $\sigma$ . \*Ages were calculated from  $^{206}$ Pb/ $^{238}$ U ratio corrected for common Pb using the  $^{207}$ Pb method (see Williams, 1998). \*Calculated ages are reported at 95% confidence level and include systematic errors added in quadrature.

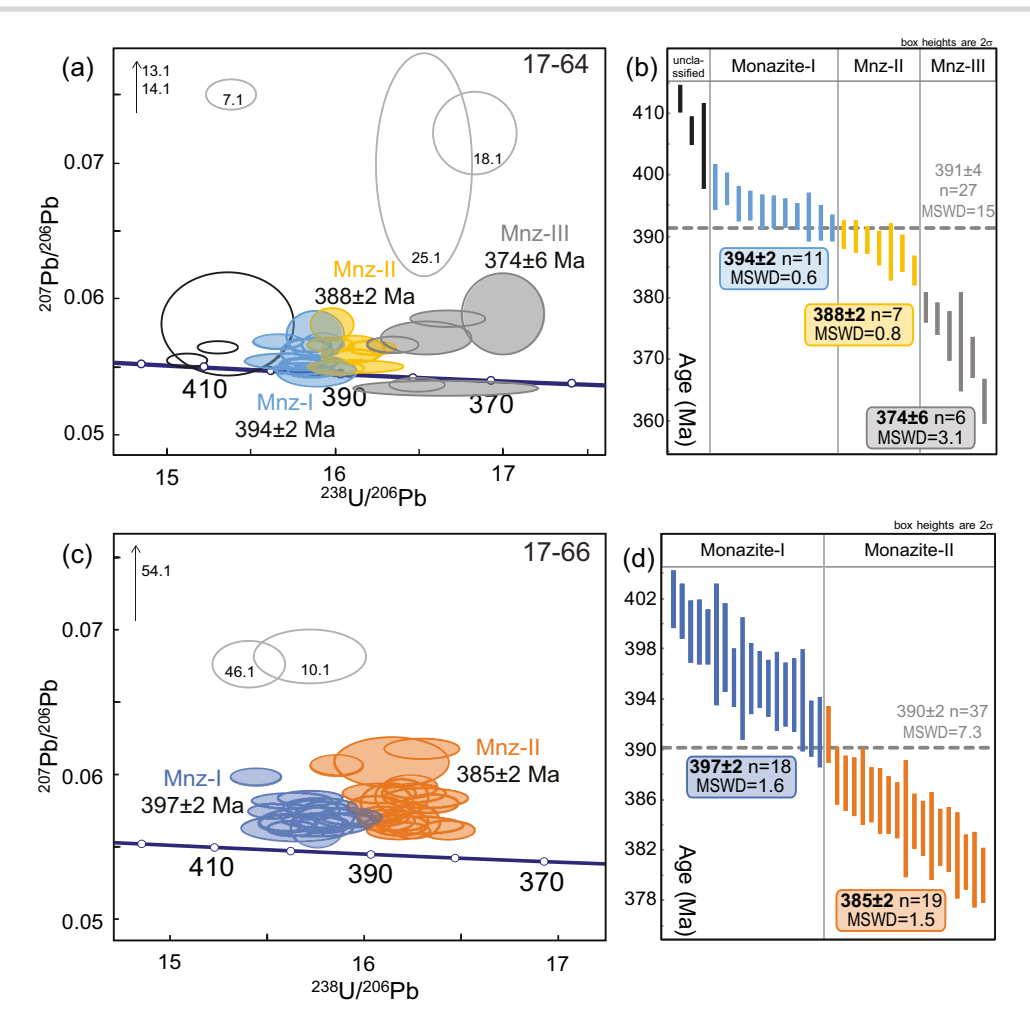


Fig. 14. Tera-Wasserburg plots of U/Pb data with 2σ error ellipses: (a) garbenschist 17-64 and (c) metapelite 17-66. Colored ellipses represent different monazite-populations and unfilled ellipses are not used in the date calculation. (b), (d) Plots of age distribution also delineate textural groups. MSWD is the mean square of weighted deviates. Analyses marked in black for sample 17-64 are interpreted as a mixed date between the detrital monazite core and the metamorphic rim.

lower Th (15587-27439 ppm) and moderate Y (2951-10 376 ppm) (Fig. 13f and h). It forms rims on Monazite-I (Fig. 12a, c, d, e and g) or occurs as separate grains in the matrix (Fig. 12f). Trace element patterns of dated monazite are the same for both chemical domains (Fig. 13b), with LREE enrichment and HREE depletion. A moderately negative Eu anomaly (Eu\* = 0.26-0.41) is observed. Monazite-I from sample 17-66 defines a weighted mean  $^{206}\text{Pb}/^{238}\text{U}$  age of  $397 \pm 2$  Ma (n = 18, MSWD = 1.6, Fig. 14c and d, Table 6), whereas Monazite-II gives an age of  $385 \pm 2$  Ma (n=19, MSWD=1.5,Fig. 14c and d).

#### DISCUSSION

Phase equilibrium modeling together with conventional and QuiG thermobarometry applied to the schists of the PBA reveal that this complex was metamorphosed at conditions of 480-650°C at pressures between 0.6 GPa and 0.9 GPa. The geochronological results demonstrate that the rocks have experienced several episodes of monazite growth in Middle to Late Devonian. The detailed

petrological studies together with in-situ monazite U-Pb dating establish a P–T–t path for the study area, which is summarized in Fig. 15. These results provide an important frame of reference for understanding the metamorphic evolution of the PBA in relation to the accretionary history of the Pearya terrane.

#### P-T-t path and monazite reaction history

The textural observations, mineral chemistry, X-ray maps and trace element geochemistry reveal typical features of a prograde metamorphic evolution. The high-Y garnet core and few xenotime grains within this chemical domain are evidence for xenotime breakdown parallel to the garnet-in reaction. The rapid decrease of Y from the core to the mantle suggests xenotime consumption with garnet growth (cf., Pyle et al., 2001; Spear & Pyle, 2002). QuiG isomekes together with Ti-inbiotite thermometry indicate garnet cores grew at 0.7-0.9 GPa and 540-600°C for garnet schist 17-66 and 0.7-0.8 GPa and 480-520°C for garbenschist 17-64 (Fig. 15, stage 1). The pseudosection model of 17-66 gives slightly different P-T conditions for garnet core formation of

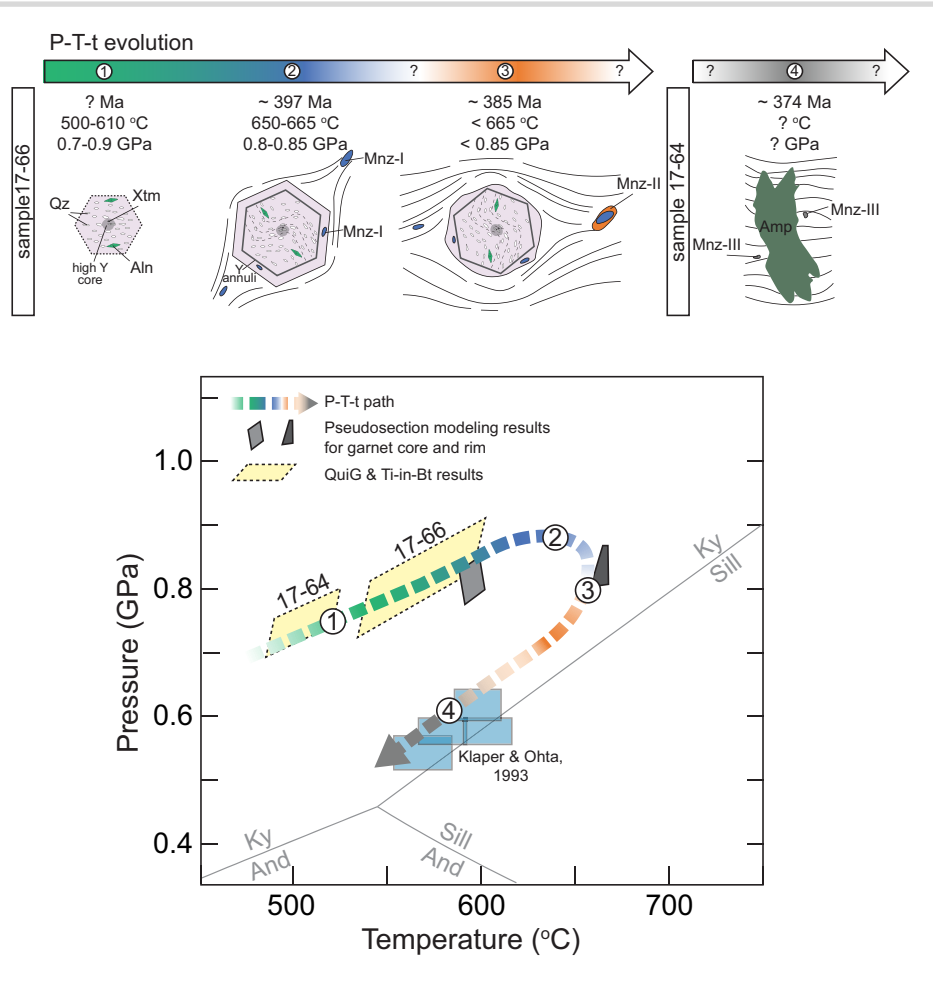


**Fig. 15.** Summary of metamorphic evolution based on phase equilibrium modeling, QuiG thermobarometry, Ti-in-biotite thermometry and monazite petrochronology. P–T–t evolution: step 1—garnet core formation at 0.7–0.9 GPa and 500–610°C; step 2—prograde growth of Monazite-I at the expense of allanite to reach peak P conditions of ~0.8–0.85 GPa and 650–665°C in the Middle Devonian; step 3—Monazite-II formation after peak-P condition (<0.85 GPa and <665°C) in middle Devonian; step 4—Monazite-III growth in the garbenschist during a late stage of retrogression. Aluminosilicate stability fields from Pattison (1992).

0.76–0.82 GPa and 585–600°C (Fig. 15, stage 2). The effective bulk composition and intersecting isopleths indicate garnet rim growth under peak conditions at  $\sim$ 0.79–0.85 GPa and 650–665°C. The garnet rims are inclusion-poor, thus QuiG thermobarometry could not be used for estimating P–T conditions of rim growth. Our estimates of peak conditions are marginally hotter and significantly higher pressure than previous work (600°C and 0.6 GPa; Klaper & Ohta, 1993).

Allanite and monazite occur together and their textural relationships are in agreement with literature examples from garnet-bearing schists (e.g. Yang & Pattison, 2006; Spear & Pyle, 2002; Skrzypek et al., 2018). Allanite occurs as inclusions in the garnet core, whereas monazite is present in the rim, thus providing additional evidence for a temperature increase during garnet growth. The monazite forming reaction most likely involved allanite and a P-bearing phase like apatite. X-ray maps of Y in garnet show enrichment at the rims, suggesting Y-bearing phase breakdown (e.g. Yang & Pattison, 2006)—in this case allanite. The monazite inclusions in garnet (outside the Y annuli) as well as cores of matrix monazite, Monazite-I, yield a weighted average

U-Pb age of  $397 \pm 2$  Ma (n = 18, MSWD = 1.6, Fig. 14b) for sample 17-66 and  $394 \pm 2$  Ma (n=11, MSWD=0.6, Fig. 14a) for the garbenschist 17-64. Based on the textural observations, this age is interpreted as prograde monazite crystallization at the expense of allanite at peak P conditions (~0.79-0.85 GPa and 650-665°C, stage 2 on Fig. 15) in the Middle Devonian. Monazite-I was rotated and followed by growth of Monazite-II parallel to the foliation (Fig. 15). Monazite-II forms single grains or overgrowths on rotated matrix Monazite-I cores. The textural observations suggest that Monazite-II grew after peak-P (<0.85 GPa and <665°C, stage 3 on Fig. 15) in the Middle Devonian; however, it is challenging to pinpoint the exact P-T conditions. Monazite-II yields the age of  $388 \pm 2 \text{ Ma} \text{ (n = 7, MSWD = 0.8, Fig. 14a)} \text{ for sample 17-64}$ and  $385 \pm 2$  Ma (n = 19, MSWD = 1.5, Fig. 14b) for sample 17-66. The reaction responsible for the formation of Monazite-II was most likely an allanite, apatite and/or Monazite-I consuming reaction, since allanite is still present in the matrix as a metastable phase. The reason for the Monazite-II growth is unclear, but it is probably a fluid driven reaction during deformation. Monazite-III is present only in the garbenschist sample

and defines the age of  $374 \pm 6$  Ma (n=6, MSWD=3.1, Fig. 14a). This domain could have grown during a late stage of retrogression due to fluid-rock interaction, which is demonstrated by the growth of amphibole. Fluid availability during retrogression is consistent with emplacement of leucocratic dikes that crosscut the amphibolite-facies schistosity in the PBA at  $369 \pm 6$  Ma (see Supplementary Appendix 1 and Fig. S2). The lack of Monazite-III in sample 17-66 may be evidence for heterogenous deformation and fluid activity.

## Application of quartz-in-garnet barometer to garbenschist

The PBA apparently experienced heterogenous fluid flow after the peak of metamorphism. Sample 17-66 does not show any retrograde features, whereas 17-64 contains abundant, randomly oriented amphibole, thus suggesting garben growth under post-peak metamorphic conditions. This study acts as a natural laboratory and testing area for further application of QuiG thermobarometry. QuiG thermobarometry applied to the garbenschist provides P estimates of metamorphic conditions in a lithology for which conventional, equilibriumbased techniques have limited use (i.e. the equilibrium state is not assured). Garbenschists commonly occur in metamorphic terranes, but most studies do not use them for thermobarometry because of the difficulties in obtaining P-T conditions of their formation. This study shows that QuiG thermobarometry can be used to estimate the early metamorphic conditions of porphyroblast growth in garbenschists (Figs. 9 and 15). A recent study of Cesare et al. (2021) shows that post-entrapment shape modifications can affect elastic thermobarometry. However, quartz in the studied garbenschist does not show evidence of post-entrapment adjustment (e.g. negative crystal shapes). Additionally, the temperatures recorded by the PBA are below 700°C (Fig. 15). The peak P obtained by QuiG thermobarometry for the metapelite sample, 17-66, is slightly higher than the results of the pseudosection modelling for the garnet core. QuiG commonly returns crystallization pressures that are higher than those obtained from phase equilibrium modelling (e.g. Spear & Wolfe, 2020) that may result from errors related to the thermodynamic modelling and/or overstepping of the garnet-in reaction (e.g. Castro & Spear, 2017; Wolfe & Spear, 2018; Nagurney et al., 2021). Garnet overstepping is a plausible explanation for PBA rocks, but requires further, extensive studies which are beyond the scope of this contribution.

# Implications for the tectonic history

The Ordovician volcaniclastic schists of the PBA, including the unusual garnet-kyanite-staurolite garbenschist, are characteristic of an arc environment. Fragments of Ordovician arcs, (e.g. the Kulutingwak formation; Bjørnerud, 1991), the Fire Bay formation (Koch et al., 2022) and the Mount Rawlinson complex (Trettin, 1998) are strung out along a series of east-striking strike-slip faults

south of the Pearva terrane (Fig. 1). The PBA displays the highest grade of metamorphism seen along the southern margin of Pearya. When taken together with the isograd pattern, the age of the metamorphism gives the best indication of the time of accretion of the Pearya terrane to the Ordovician arcs and Danish River flysch, as well as the deep water part of the Franklinian margin. The highgrade rocks of the PBA are metamorphic equivalents of the sub-greenschist facies Kulutingwak formation (Fig. 1; Klaper & Ohta, 1993; Trettin, 1998), which is found along the Kulutingwak and the Emma Fiord fault zones. Serpentinite blocks and carbonate olistoliths mixed with a variety of schist and amphibolite in the PBA suggest deposition in a subduction environment. Selverstone et al. (1984) argued for subduction zone metamorphism to explain a similar garbenschist assemblage in the Tauern window, Austrian Alps, but the peak temperature was 100°C lower and the pressure was marginally higher (1.0 GPa) than the PBA. An Eclogite Zone structurally beneath the garbenschist unit with P = 0.9-1.3 GPa points to subduction in the Tauern window as well; however, Smye et al. (2011) consider the possibility of a Barrovian overprint due to later overthrusting of Austroalpine units. Nevertheless, the peak conditions of 665°C at 0.78–0.85 GPa for the PBA are too hot and marginally too low pressure for metamorphism in a subduction zone. The Devonian monazite in the PBA, which grew on the prograde and retrograde clockwise P-T path, is also incompatible with Ordovician subduction.

The medium temperature/medium pressure (MT/MP) conditions of the PBA, i.e. 650°C at ≤0.9 GPa, are more characteristic of a Barrovian metamorphic history. Our monazite dating shows that garnet grew on a prograde path over a period of ≈12 Myr from 397–385 Ma. This period falls outside Viete & Lister's (2017) 10 Myr threshold for short duration regional metamorphism, but still requires a localized heat source in a time frame much less than that required for conductive heating in a continent-continent collision (e.g. England & Thompson, 1984; Dewey, 2005). The closely spaced, steep, parallel isograd surfaces (Fig. 2b) indicate a heat source to the northwest that was applied after the main fabric-forming event (Klaper & Ohta, 1993; Figs 4 and 6). The localized nature of the Barrovian metamorphism of the PBA indicates either a heat source from nearby magma emplacement or a 'hot iron' of obducted arc and thin ophiolitic forearc (Ryan & Dewey, 2019). Shear heating along the emplacement structure is unlikely to increase the temperature much beyond 20°C (e.g. Platt, 2015). The lack of ophiolite and the age difference between metamorphism and the arc fragments in the PBA argue against a hot iron mechanism associated with the Ordovician arc system.

The crystalline basement of the composite Pearya terrane lies directly northwest of the PBA and its proximity suggests a causal relationship between accretion and Barrovian metamorphism (Klaper & Ohta, 1993; Trettin, 1998). For example, granulite facies crust forming a

hot orogenic root was thrust over the Moravian zone of the Bohemian massif to produce peak Barrovian conditions (Štípská et al., 2015) similar to those observed in the PBA. The 485-440 Ma magmatic rocks and Ordovician metamorphism associated with the M'Clintock collisional event within the Pearya terrane (McClelland et al., 2012; Estrada et al., 2018; Majka et al., 2021) are too old to be considered a viable heat source for the PBA metamorphism. On the other hand, evidence for metamorphism and granitic magmatism in the Pearya basement at 365-340 Ma (Trettin, 1998; Estrada et al., 2018) is too young to be directly related to the PBA metamorphism. The P-T conditions of the adjacent quartzofeldspathic gneisses of Pearya have not been determined, but they do not appear to exceed amphibolite facies and were probably not hot enough to produce the metamorphic isograds observed in the PBA. Another possible heat source may be Devonian magmas intruded into the Pearya terrane or other Ordovician arc fragments and brought into contact with a fragment of an Ordovician arc containing the PBA. The Cape Woods pluton (Fig. 1) is a plausible example of such a magma: it has a U-Pb titanite intrusive age of  $390 \pm 10$  Ma (Trettin et al., 1987) and a contact aureole with scattered kyanite and staurolite adjacent to the pluton (Frisch, 1974). No intrusion similar to the Cape Woods pluton is seen directly northwest of the PBA today, but it could have been excised by later brittle faults in the Cenozoic. The Bourne Complex exposed on the Kleybolte Peninsula (Fig. 1) includes calc-alkaline intermediate volcanic rocks with an average age of  $380 \pm 14$  Ma based on <sup>40</sup>Ar/<sup>39</sup>Ar data (Henry, 1981; Trettin, 1998). This section may represent remnants of a Devonian arc system, the roots of which could result in Barrovian metamorphism if emplaced next to the PBA. The Bourne Complex is juxtaposed along the steep Kleybolte fault with serpentinized ultramafic rocks of unknown age, the Danish River Formation and Carboniferous units in a setting similar to the PBA. In either scenario—magma emplacement or hot iron-like juxtaposition with the deeper levels of a Devonian magmatic complex—it is clear that the present day juxtaposition of the Pearya terrane against the PBA does not reflect the primary relationship at the time of Barrovian metamorphism. The Petersen Bay Fault Zone experienced intense Cenozoic brittle faulting with an unknown amount of displacement (Piepjohn et al., 2013; Piepjohn & von Gosen, 2018). An approximately 250-300 m thick package of cataclasite, derived primarily from the quartzofeldspathic gneiss of Pearya and observed just 1 km SW of the studied outcrop, indicates significant late displacement. Thus, the causal relationship between Pearya terrane accretion and Barrovian metamorphism of the PBA (Klaper & Ohta, 1993) requires significant post-accretion modification to establish the present day relationships.

Metamorphism associated with the development of the kyanite-staurolite-garnet garbenschist appears to be a common occurrence in collisional to accretionary settings that involve magmatic rocks that can form a

Barrovian heat source and bulk compositions appropriate for the unusual low-variance assemblage. The Tauern window garbenschist formed in response to subduction of volcanic protoliths to 1 GPa and 530°C, followed by exhumation and continued heating to 0.7 GPa and 550°C (Selverstone et al., 1984; Selverstone, 1985, 1993). Preservation of the relatively cool system can be attributed to the absence of arc magmatism and short duration of the subduction to exhumation cycle (Smye et al., 2011). The kyanite-staurolite-garnet-amphibole assemblage observed in the Pie de Palo complex, Argentina formed at conditions ranging from 0.9–1.3 GPa and 600-638°C within a fore arc setting during collision of the Precordillera terrane (Casquet et al., 2001; Mulcahy et al., 2011). Structurally higher units that experienced deformation at 1.2-1.3 GPa and 735-800°C in the presence of melt represent deeper portions of the longlived arc-continent collision prior to the onset of strikeslip terrane displacement (Mulcahy et al., 2011; Tholt et al., 2021). Similarly, garbenschist formed at 0.87 GPa and 545°C during underthrusting of the Alexander terrane in an intra-arc setting (McClelland et al., 1991) was followed by margin parallel displacement on an intra-arc dextral shear zone (McClelland & Mattinson, 2000). Metamorphism in the PBA appears to represent burial to 0.8-0.9 GPa and Barrovian metamorphism associated with the final arc-related magmatic event within the Pearya terrane. The timing of PBA metamorphism suggests that underthrusting of Ordovican arc fragments inboard of the Pearya terrane within a transpressional setting (McClelland et al., 2022) occurred after its accretion to and before contraction of the Ellesmerian orogeny initiated at ≈360 Ma (Latest Famenian to Tournasian; Piepjohn et al., 2013). In all of these settings, units that experienced burial-related Barrovian metamorphism are rapidly exhumed and variably overprinted by post collisional deformation at shallower crustal levels.

#### CONCLUSIONS

This study shows that garbenschist-type rocks that commonly have textural evidence indicating chemical and microstructural disequilibrium can be used for interpreting metamorphic evolution by combining QuiG with other thermobarometric and geochronological approaches. Quartz in garnet Raman thermobarometry and Ti-in-biotite thermometry produced peak MT/MP conditions of 650°C and ≤0.9 GPa that are consistent with results of phase equilibrium modelling of nearby well-equilibrated and unaltered garnet-mica schists. The QuiG results help define the prograde path leading up to the peak temperatures recorded by the pseudosection models from adjacent garnet-mica schists. The original P estimates from the PBA (Klaper & Ohta, 1993) were based on conventional thermobarometry and are considerably lower than those provided by QuiG. We suggest that the lower pressures were realized during exhumation, which still took place in the kyanite stability field. QuiG has the potential to improve the P estimates and P-T paths for garbenschist in general because the method is not based on assumptions of chemical equilibrium inherent in conventional thermobarometry or thermodynamic modeling.

Tying geochronologic information to the P-T path remains challenging, but garnet-bearing assemblages containing monazite are useful because of inclusionmatrix relationships and partitioning of REE elements such as Y. Three different monazite domains were identified and dated in this study. Monazite I grew at  $397 \pm 2$  Ma (sample 17-66) and  $394 \pm 2$  Ma (sample 17-64) from allanite after the garnet core formed; this age is the best approximation of the timing of accretion of Pearya to the Ordovician arcs and Siluro-Devonian flysch. Further allanite reaction produced Monazite II at 388 ± 2 Ma (sample 17-66) and  $385 \pm 2$  Ma (sample 17-66) with lower Th that overgrew Monazite I and formed elongate matrix grains parallel to the dominant schistosity. A late phase of lower Y Monazite III grew at 374 ± 6 Ma in the matrix of the garbenschist probably due to fluid influx during exhumation. The in-situ dating and analysis of monazite chemistry is essential for relating the textural position to other important phases like garnet to establish the P-T-t

Closely spaced isograds show that temperature and pressure increased to the northwest, requiring a heat source in the direction of the adjacent Pearya terrane. The amphibolite facies gneiss of Pearya was probably not hot enough to produce the prograde metamorphism seen in the PBA over a relatively short (12 Myr) time frame. We speculate that Devonian magmas in the Pearya terrane caused the metamorphism and were later excised by the Cenozoic strike-slip fault that separates the two areas. Although there is no a priori reason to expect the tectonic settings of the unusual garbenschist assemblages to be the same, there are some striking similarities among these occurrences. The garnet-kyanite-staurolite garbenschists from Ellesmere Island, Austria, Argentina and Alaska all record complicated MT/MP metamorphic histories associated with burial and exhumation in collisional and accretionary settings. All but the Tauern example were fragments formed in a transpressional regime that was modified by significant later translation.

### **FUNDING**

We thank the German Federal Institute for Geosciences and Natural Resources for the invitation to participate in the 2017 expedition to Ellesmere Island, and for funding and organizing the fieldwork. The analytical work for this project was funded by the National Science Foundation grant EAR 1650022 to Gilotti and McClelland, including support of a one-year post doc for Kośmińska at the University of Iowa. Gilotti acknowledges a 2021–2022 Fulbright US Scholar Award to visit AGH-UST in Kraków, Poland, for the writing-up phase of the project.

#### SUPPLEMENTARY DATA

Supplementary data are available at Journal of Petrology online.

## **ACKNOWLEDGEMENTS**

The Polar Continental Shelf Project out of Resolute Bay, Canada, provided logistical support for the expedition. We are grateful to Kenny Horkley for technical help with the electron microprobe analysis and to Frank Spear and Oliver Wolfe for help with Raman analysis. Justin Strauss and Karol Faehnrich are thanked for many productive discussions during and after fieldwork for this study. Comments from Adrian Castro and an anonymous reviewer helped improve the manuscript.

## References

- Aleinikoff, J. N., Schenck, W. S., Plank, M. O., Srogi, L., Fanning, C. M., Kamo, S. L. & Bosbyshell, H. (2006). Deciphering igneous and metamorphic events in high-grade rocks of the Wilmington complex, Delaware: morphology, cathodoluminescence and backscattered electron zoning, and SHRIMP U-Pb geochronology of zircon and monazite. Geological Society of America Bulletin 118, 39-64. https://doi.org/10.1130/B25659.1.
- Aleinikoff, J. N., Grauch, R. I., Mazdab, F. K., Kwak, L., Fanning, C. M. & Kamo, S. L. (2012). Origin of an unusual monazite-xenotime gneiss, Hudson highlands, New York: SHRIMP U-Pb geochronology and trace element geochemistry. American Journal of Science 312, 723-765. https://doi.org/10.2475/07.2012.02.
- Alvaro, M., Mazzucchelli, M. L., Angel, R. J., Murri, M., Campomenosi, N., Scambelluri, M., Nestola, F., Korsakov, A., Tomilenko, A. A., Marone, F. & Morana, M. (2020). Fossil subduction recorded by quartz from the coesite stability field. Geology 48, 24-28. https:// doi.org/10.1130/G46617.1.
- Angel, R. J., Mazzucchelli, M. L., Alvaro, M., Nimis, P. & Nestola, F. (2014). Geobarometry from host-inclusion systems: the role of elastic relaxation. American Mineralogist 99, 2146-2149. https://doi.org/10.2138/am-2014-5047.
- Angel, R. J., Nimis, P., Mazzucchelli, M. L., Alvaro, M. & Nestola, F. (2015). How large are departures from lithostatic pressure? Constraints from host-inclusion elasticity. Journal of Metamorphic Geology 33, 801-813. https://doi.org/10.1111/jmg.12138.
- Angel, R. J., Alvaro, M., Miletich, R. & Nestola, F. (2017). A simple and generalised P-T-V EoS for continuous phase transitions, implemented in EosFit and applied to quartz. Contributions to Mineralogy and Petrology 172(5), 1-15. https://doi.org/10.1007/ s00410-017-1349-x.
- Angel, R. J., Murri, M., Mihailova, B. & Alvaro, M. (2019). Stress, strain and Raman shifts. Zeitschrift Fur Kristallographie—Crystalline Materials **234**(2), 129–140. https://doi.org/10.1515/zkri-2018-2112.
- Arnold, J., Powell, R. & Sandiford, M. (2000). Amphibolites with staurolite and other aluminous minerals: calculated mineral equilibria in NCFMASH. Journal of Metamorphic Geology 18, 23-40. https://doi.org/10.1046/j.1525-1314.2000.00236.x.
- Ashley, K. T., Caddick, M. J., Steele-MacInnis, M. J., Bodnar, R. J. & Dragovic, B. (2014). Geothermobarometric history of subduction recorded by quartz inclusions in garnet: quartz inclusion barometry. Geochemistry, Geophysics, Geosystems 15, 350-360. https://doi.org/10.1002/2013GC005106.

- Barth, A. P. & Wooden, J. L. (2006). Timing of magmatism following initial convergence at a passive margin, southwestern U.S. Cordillera, and ages of lower crustal magma sources. Journal of Geology 114, 231-245. https://doi.org/10.1086/499573.
- Barth, A. P. & Wooden, J. L. (2010). Coupled elemental and isotopic analyses of polygenetic zircons from granitic rocks by ion microprobe, with implications for melt evolution and the sources of granitic magmas. Chemical Geology 277, 149-159. https://doi.org/10.1016/j.chemgeo.2010.07.017.
- Bjørnerud, M. G. (1991). Structural evolution of the Kulutingwak zone, northwestern Ellesmere Island, Northwest Territories: the northern edge of Paleozoic North America? Current Research: Geological Survey of Canada, Paper 91-1(E), 187-195.
- Bjørnerud, M. G. & Bradley, D. C. (1992) Silurian foredeep and accretionary prism in northern Ellesmere Island: Implications for the nature of the Ellesmerian orogeny. In: Thurston D. K. & Fujita K. (eds) Proceedings of the International Conference on Arctic Margins: U.S. Mineral Management Service Outer Continental shelf Study MMS94-0040, pp.129-133.
- Bonazzi, M., Tumiati, S., Thomas, J. B., Angel, R. J. & Alvaro, M. (2019). Assessment of the reliability of elastic geobarometry with quartz inclusions. Lithos 350-351, 105201. https://doi.org/10.1016/j.lithos.2019.105201.
- Casquet, C., Baldo, E., Pankhurst, R. J., Rapela, C. W., Galindo, C., Fanning, C. M. & Saavedra, J. (2001). Involvement of the Argentine Precordillera terrane in the Famatinian mobile belt: U-Pb SHRIMP and metamorphic evidence from the Sierra de Pie de Palo. Geology 29, 703-706. https://doi.org/10.1130/0091-7613(2001)029&#x003 C;0703:IOTAPT>2.0.CO;2.
- Castro, A. E. & Spear, F. S. (2017). Reaction overstepping and re-evaluation of peak P-T conditions of the blueschist unit Sifnos, Greece: implications for the Cyclades subduction zone. International Geology Review 59, 548-562. https://doi.org/10.1080/00206814.2016.1200499.
- Catlos, E. J., Gilley, L. D. & Harrison, T. M. (2002). Interpretation of monazite ages obtained via in situ analysis. Chemical Geology 188, 193-215. https://doi.org/10.1016/S0009-2541(02)00099-2.
- Cesare, B., Parisatto, M., Mancini, L., Peruzzo, L., Franceschi, M., Tacchetto, T., Reddy, S., Spiess, R., Nestola, F. & Marone, F. (2021). Mineral inclusions are not immutable: evidence of post-entrapment thermally-induced shape change of quartz in garnet. Earth and Planetary Science Letters 555, 116708. https://doi.org/10.1016/j.epsl.2020.116708.
- Connolly, J. A. D. (1990). Multivariable phase diagrams; an algorithm based on generalized thermodynamics. American Journal of Science 290, 666-718. https://doi.org/10.2475/ajs.290.6.666.
- Connolly, J. A. D. (2005). Computation of phase equilibria by linear programming: a tool for geodynamic modeling and its application to subduction zone decarbonation. Earth and Planetary Science Letters 236, 524-541. https://doi.org/10.1016/j.epsl.2005.04.033.
- Crawford, A. J., Falloon, T. J. & Eggins, S. (1987). The origin of island arc basalts. Contributions to Mineralogy and Petrology 97, 417-430. https://doi.org/10.1007/BF00372004.
- Dewey, J. F. (2005). Orogeny can be very short. Proceedings of the National Academy of Sciences 102, 15286-15293. https://doi.org/10.1073/pnas.0505516102.
- Dewing, K., Hadlari, T., Pearson, D. G. & Matthews, W. (2019). Early Ordovician to early Devonian tectonic development of the northern margin of Laurentia, Canadian Arctic Islands. Geological Society of America Bulletin 131, 1075-1094. https://doi.org/10.1130/B35017.1.
- Dumond, G., Goncalves, P., Williams, M. L. & Jercinovic, M. J. (2015). Monazite as a monitor of melting, garnet growth and feldspar

- recrystallization in continental lower crust. Journal of Metamorphic Geology 33(7), 735-762. https://doi.org/10.1111/jmg.12150.
- Enami, M., Nishiyama, T. & Mouri, T. (2007). Laser Raman microspectrometry of metamorphic quartz: a simple method for comparison of metamorphic pressures. American Mineralogist 92, 1303-1315. https://doi.org/10.2138/am.2007.2438.
- Engi, M. (2017) Petrochronology based on REE-minerals: monazite, allanite, xenotime, apatite. In: Kohn M. J., Engi M. & Lanari P. (eds) Petrochronology: Methods and Applications, Vol. 83, pp. 365–418, https://doi.org/10.1515/9783110561890-013.
- Engi, M., Lanari, P. & Kohn, M. J. (2017) Significant ages—an introduction to petrochronology. In: Kohn M. J., Engi M. & Lanari P. (eds) Petrochronology: Methods and Applications, Vol. 83, pp. 1-12, https://doi.org/10.1515/9783110561890-002.
- England, P. C. & Thompson, A. B. (1984). Pressure-temperature-time paths of regional metamorphism I. heat transfer during the evolution of regions of thickened continental crust. Journal of Petrology 25, 894-928. https://doi.org/10.1093/petrology/25.4.894.
- Estrada, S., Mende, K., Gerdes, A., Gärtner Hofmann, M., Spiegel, C., Damaske, D. & Koglin, N. (2018). Proterozoic to Cretaceous evolution of the western and central Pearya terrane (Canadian High Arctic). Journal of Geodynamics 120, 45-76. https://doi.org/10.1016/j.jog.2018.05.010.
- Evans, T. P. (2004). A method for calculating effective bulk composition modification due to crystal fractionation in garnetbearing schist; implications for isopleth thermobarometry. Journal of Metamorphic Geology 22, 547-557. https://doi.org/10.1111/ j.1525-1314.2004.00532.x.
- Faryad, S. W. & Hoinkes, G. (2006). Reaction textures in Al-rich metabasite: implication for metamorphic evolution of the eastern border of the Middle Austroalpine basement units. Lithos 90, 145–157. https://doi.org/10.1016/j.lithos.2006.02.005.
- Fatehi, H., Ahmadipour, H., Kuzuo, N. & Moeinzadeh, H. (2017). Feather-like hornblende aggregates in the phyllites from the southern Sanandaj-Sirjan zone, Iran; their origin and mode of formation. Turkish Journal of Earth Sciences 26, 421-440. https://doi.org/10.3906/yer-1702-11.
- Forshaw, J. B. & Pattison, D. R. M. (2021). Ferrous/ferric (Fe<sup>2+</sup>/Fe<sup>3+</sup>) partitioning among silicates in metapelites. Contributions to Mineralogy and Petrology 176, 63. https://doi.org/10.1007/ s00410-021-01814-4.
- Foster, G., Kinny, P., Vance, D., Prince, C. & Harris, N. (2000). The significance of monazite U-Th-Pb age data in metamorphic assemblages; a combined study of monazite and garnet chronometry. Earth and Planetary Science Letters 181, 327-340. https://doi.org/10.1016/S0012-821X(00)00212-0.
- Frisch, T. (1974). Metamorphic and plutonic rocks of northernmost Ellesmere Island, Canadian Arctic Archipelago. Geological Survey of Canada Bulletin 229, 87.
- Gonzalez, J. P., Thomas, J. B., Baldwin, S. L. & Alvaro, M. (2019). Quartzin-garnet and Ti-in-quartz thermobarometry: methodology and first application to a quartzofeldspathic gneiss from eastern Papua New Guinea. Journal of Metamorphic Geology 37, 1193–1208. https://doi.org/10.1111/jmg.12508.
- Hallett, B. W. & Spear, F. S. (2015). Versatile Monazite: Resolving Geological Records and Solving Challenges in Materials Science. Monazite, zircon, and garnet growth in migmatitic pelites as a record of metamorphism and partial melting in the East Humboldt Range, Nevada. American Mineralogist 100, 951-972. https:// doi.org/10.2138/am-2015-4839.
- Harvey, K. M., Penniston-Dorland, S. C., Kohn, M. J. & Piccoli, P. M. (2021). Assessing P-T variability in mélange blocks from the Catalina schist: is there differential movement at the

- subduction interface? Journal of Metamorphic Geology 39, 271–295. https://doi.org/10.1111/jmg.12571.
- Hawthorne, F. C., Oberti, R., Harlow, G. E., Maresch, W. V., Martin, R. F., Schumacher, J. C. & Welch, M. D. (2012). Nomenclature of the amphibole supergroup. American Mineralogist 97, 2031-2048. https://doi.org/10.2138/am.2012.4276.
- Helms, T. S., McSween, H. Y., Jr., Labotka, T. C. & Jarosewich, E. (1987). Petrology of a Georgia Blue Ridge amphibolite unit with hornblende + gedrite + kyanite + staurolite. American Mineralogist **72**, 1086–1096.
- Henry, A. S. (1981) The petrochemistry and origin of the Bourne Complex, northwestern Ellesmere Island, Canada. Unpublished B.Sc., Honours, thesis, Department of Geology, Dalhousie University, Halifax, Nova Scotia, p. 120.
- Henry, D. J., Guidotti, C. V. & Thomson, J. A. (2005). The Tisaturation surface for low-to-medium pressure metapelitic biotites: implications for geothermometry and Ti-substitution mechanisms. American Mineralogist 90, 316-328. https://doi. org/10.2138/am.2005.1498.
- Hodges, K. V. & Spear, F. S. (1982). Geothermometry, geobarometry and the Al2SiO5 triple point at Mt. Moosilauke New Hampshire. American Mineralogist 67, 1118-1134.
- Holland, T. & Powell, R. (2003). Activity-composition relations for phases in petrological calculations: an asymmetric multicomponent system. Contributions to Mineralogy and Petrology 145, 492–501. https://doi.org/10.1007/s00410-003-0464-z.
- Holland, T. J. B. & Powell, R. (2011). An improved and extended internally consistent thermodynamic dataset for phases of petrological interest, involving a new equation of state for solids. Journal of Metamorphic Geology 29, 333-383. https://doi.org/10.1111/j.1525-1314.2010.00923.x.
- Klaper, E. M. (1992). The Paleozoic tectonic evolution of the northern edge of North America: a structural study of northern Ellesmere Island, Canadian Arctic archipelago. Tectonics 11, 854-870. https://doi.org/10.1029/92TC00277.
- Klaper, E. M. & Ohta, Y. (1993). Paleozoic metamorphism across the boundary between the Clements Markham fold belt and the Pearya terrane in northern Ellesmere Island, Canadian Arctic archipelago. Journal Canadien des Dciences de la Terre 30, 867-880. https://doi.org/10.1139/e93-072.
- Koch, M. M., Feahnrich, K., McClelland, W. C., Crowley, J. L., Melchin, M. J., Beranek, L. P. & Strauss, J. V. (2022) Age and significance of the Fire Bay formation: An Ordovician arc fragment within the Clements Markham Belt, northwest Ellesmere Island, Canada. Canadian Journal of Earth Science. https://doi.org/10.1139/ cjes-2021-0129.
- Kohn, M. J. (2014). "Thermoba-Raman-try": calibration of spectroscopic barometers and thermometers for mineral inclusions. Earth and Planetary Science Letters 388, 187–196. https://doi. org/10.1016/j.epsl.2013.11.054.
- Kohn, M. J., Wieland, M. S., Parkinson, C. D. & Upreti, B. N. (2005). Five generations of monazite in Langtang gneisses: implications for chronology of the Himalayan metamorphic core. Journal of Metamorphic Geology 23, 399-406. https://doi.org/10.1111/j.1525-1314.2005.00584.x.
- Kośmińska, K., Spear, F. S., Majka, J., Faehnrich, K., Manecki, M., Piepjohn, K. & Dallmann, W. K. (2020). Deciphering late Devonian-early carboniferous P-T-t path of mylonitized garnet-mica schists from Prins Karls Forland, Svalbard. Journal of Metamorphic Geology 38, 471-493. https://doi.org/10.1111/jmg.12529.
- Kuyumjian, R. M. (1998). Kyanite-staurolite ortho-amphibolite from the Chapada region, Goiás, Central Brazil. Mineralogical Magazine 62, 501–507. https://doi.org/10.1180/002646198547873.

- Kylander-Clark, A. R. C., Hacker, B. R. & Cottle, J. M. (2013). Laserablation split-stream ICP petrochronology. Chemical Geology 345, 99-112. https://doi.org/10.1016/j.chemgeo.2013.02.019.
- Lanari, P. & Duesterhoeft, E. (2019). Modeling metamorphic rocks using equilibrium thermodynamics and internally consistent databases: past achievements, problems and perspectives. Journal of Petrology 60, 19-56. https://doi.org/10.1093/petrology/egy105.
- Lanari, P. & Engi, M. (2017) Local bulk composition effects on mineral assemblages. In: Kohn M. J., Engi M. & Lanari P. (eds) Petrochronology: Methods and Applications, Vol. 83, pp. 55-102, https://doi.org/10.1515/9783110561890-004.
- Ludwig, K. R. (2009). Squid 2, a user's manual. Berkeley Geochronology Center Special Publication No. 5, 110.
- Ludwig, K. R. (2012). Isoplot 3.75, a geochronological toolkit for excel. Berkeley Geochronology Center Special Publication No. 5, 75.
- Majka, J., Kośmińska, K., Bazarnik, J. & McClelland, W. C. (2021). The Ordovician Thores volcanic island arc of the Pearya terrane from northern Ellesmere Island formed on Precambrian continental crust. Lithos 386-387, 105999. https://doi.org/10.1016/j.lithos.2021.105999.
- Malone, S. J., McClelland, W. C., von Gosen, W. & Piepjohn, K. (2014). Proterozoic evolution of the North Atlantic-Arctic Caledonides: insights from detrital zircon analysis of metasedimentary rocks from the Pearya terrane, Canadian High Arctic. Journal of Geology 122, 623-647. https://doi.org/10.1086/677902.
- Malone, S. J., McClelland, W. C., von Gosen, W. & Piepjohn, K. (2017). The earliest Neoproterozoic magmatic record of the Pearya terrane, Canadian high Arctic: implications for Caledonian terrane reconstructions. Precambrian Research 292, 323-349. https://doi.org/10.1016/j.precamres.2017.01.006.
- Malone, S. J., McClelland, W. C., von Gosen, W. & Piepjohn, K. (2019). Detrital zircon U-Pb and Lu-Hf analysis of Paleozoic sedimentary rocks from the Pearya terrane and the Ellesmerian Fold Belt (northern Ellesmere Island): a comparison with Circum-Arctic datasets and their implications on terrane tectonics. In: Piepjohn, K., Strauss, J.V., Reinhardt, L. & McClelland, W.C. (eds.), Circum-Arctic Structural Events: Tectonic Evolution of the Arctic Margins and Trans-Arctic Links With Adjacent Orogens. Geological Society of America Special Paper 541, 231–254, https://doi.org/10.1130/2018.2541(12).
- Manzotti, P., Bosse, V., Pitra, P., Robyr, M., Schiavi, F. & Ballèvre, M. (2018). Exhumation rates in the Gran Paradiso Massif (Western Alps) constrained by in situ U–Th–Pb dating of accessory phases (monazite, allanite and xenotime). Contributions to Mineralogy and Petrology 173, 24. https://doi.org/10.1007/s00410-018-1452-7.
- McClelland, W. C. & Mattinson, J. M. (2000) Cretaceous-Tertiary evolution of the western Coast Mountains, central southeastern Alaska. In: Stowell H. H. & McClelland W. C. (eds) Tectonics of the Coast Mountains, Southeastern Alaska and British Columbia. Geological Society of America Special Paper, Vol. 343, pp. 159-182, https://doi.org/10.1130/0-8137-2343-4.159.
- McClelland, W. C., Anovitz, L. M. & Gehrels, G. E. (1991). Thermobarometric constraints on the structural evolution of the Coast Mountains batholith, central southeastern Alaska. Canadian Journal of Earth Sciences 28, 912-928. https://doi.org/10.1139/e91-083.
- McClelland, W. C., Malone, S. J., von Gosen, W., Piepjohn, K. & Läufer, A. (2012). The timing of sinistral displacement of the Pearya Terrane along the Canadian Arctic Margin. Zeitschrift der deutschen Gesellschaft fuer Geowissenschaften 163, 251–259. https:// doi.org/10.1127/1860-1804/2012/0163-0251.
- McClelland, W. C., Strauss, J. V., Gilotti, J. A., Colpron, M., Faehnrich, K., Malone, S. J., Macdonald, F. A. & Oldow, J. S. (2021). Taters versus sliders: evidence for a long-lived history of strike-slip

- displacement along the Canadian Arctic Transform System (CATS). GSA Today 31(7), 4-11. https://doi.org/10.1130/GSATG500 A.1.
- McClelland, W. C., Strauss, J. V., Gilotti, J. A. & Colpron, M. (2022) Paleozoic evolution of the northern Laurentian margin: Evaluating links between Caledonian, Ellesmerian and Cordilleran orogens. In: Whitmeyer S., Kellett D., Williams M. & Tikoff B. (eds) Laurentia: An Evolving Continent. Geological Society of America Memoir, in press.
- Mottram, C. M., Warren, C. J., Regis, D., Roberts, N. M. W., Harris, N. B. W., Argles, T. W. & Parrish, R. R. (2014). Developing an inverted Barrovian sequence; insights from monazite petrochronology. Earth and Planetary Science Letters 403, 418-431. https://doi.org/10.1016/j.epsl.2014.07.006.
- Mulcahy, S. R., Roeske, S. M., McClelland, W. C., Jourdan, F., Iriondo, A., Renne, P. R., Vervoort, J. D. & Vujovich, G. I. (2011). Structural evolution of a composite middle to lower crustal section: the Sierra de Pie de Palo, Northwest Argentina. Tectonics 30, TC1005. https://doi.org/10.1029/2009TC002656.
- Murri, M., Mazzucchelli, M. L., Campomenosi, N., Korsakov, A. V., Prencipe, M., Mihailova, B. D., Scambelluri, M., Angel, R. J. & Alvaro, M. (2018). Raman elastic geobarometry for anisotropic mineral inclusions. American Mineralogist 103, 1869-1872.
- Nagurney, A. B., Caddick, M. J., Dragovic, B. & Busse, K. (2021). The (chemical) potential for understanding overstepped garnet nucleation and growth. American Mineralogist 106(5), 812-829. https://doi.org/10.2138/am-2021-7354.
- Palin, R. M., Searle, M. P., Waters, D. J., Horstwood, M. S. A. & Parrish, R. R. (2012). Combined thermobarometry and geochronology of peraluminous metapelites from the Karakoram metamorphic comples, North Pakistan; new insight into the tectonothermal evolution of the Baltoro and Hunza Valley regions. Journal of Metamorphic Geology 30, 793-820. https://doi.org/10.1111/j.1525-1314.2012.00999.x.
- Palin, R. M., Weller, O. M., Waters, D. J. & Dyck, B. (2016). Quantifying geological uncertainty in metamorphic phase equilibria modelling; a Monte Carlo assessment and implications for tectonic interpretations. Geoscience Frontiers 7(4), 591–607. https://doi.org/10.1016/j.gsf.2015.08.005.
- Pattison, D. R. M. (1992). Stability of andalusite and sillimanite and the Al<sub>2</sub>SiO<sub>5</sub> triple point: constraints from the Ballachulish Aureole, Scotland. The Journal of Geology 100, 423-446. https://doi.org/10.1086/629596.
- Petrík, I., Janák, M., Klonowska, I., Majka, J., Froitzheim, N., Yoshida, K., Sasinková, V., Konečný, P. & Vaculovič, T. (2019). Monazite behaviour during metamorphic evolution of a diamondbearing gneiss: a case study from the Seve Nappe Complex, Scandinavian Caledonides. Journal of Petrology 60(9), 1773–1796. https://doi.org/10.1093/petrology/egz051.
- Piepjohn, K. & von Gosen, W. (2018) Structural transect through Ellesmere Island (Canadian Arctic): superimposed Palaeozoic Ellesmerian and Cenozoic Eurekan deformation. In: Pease V. & Coakley B. (eds) Geological Society, London, Special Publications, Vol. 460. Geological Society, London, Special Publications, pp. 33-56, https://doi.org/10.1144/SP460.5.
- Piepjohn, K., von Gosen, W., Läufer, A., McClelland, W. C. & Estrada, S. (2013). Ellesmerian and Eurekan fault tectonics at the northern margin of Ellesmere Island (Canadian High Arctic). Franz Schuh 164, 81-105. https://doi.org/10.1127/1860-1804/2013/0007.
- Platt, J. P. (2015). Influence of shear heating on microstructurally defined plate boundary shear zones. Journal of Structural Geology 79, 80-89. https://doi.org/10.1016/j.jsg.2015.07.009.

- Pyle, J. M. & Spear, F. S. (2003). Four generations of accessory phase growth in low-pressure migmatites from SW New Hampshire. American Mineralogist 88, 338-351. https://doi.org/10.2138/ am-2003-2-311.
- Pyle, J. M., Spear, F. S., Rudnick, R. L. & McDonough, W. F. (2001). Monazite-xenotime-garnet equilibrium in metapelites and a new monazite-garnet thermometer. Journal of Petrology 42, 2083-2107. https://doi.org/10.1093/petrology/42.11.2083.
- Rosenfeld, J. L. (1969). Stress effects around quartz inclusions in almandine and the piezothermometry of coexisting aluminum silicates. American Journal of Science 267, 317-351. https://doi.org/10.2475/ajs.267.3.317.
- Rosenfeld, J. L. & Chase, A. B. (1961). Pressure and temperature of crystallization from elastic effects around solid inclusion minerals? American Journal of Sciences 259, 519-541.
- Rubatto, D., Chakraborty, S. & Dasgupta, S. (2013). Timescales of crustal melting in the higher Himalayan Crystallines (Sikkim, Eastern Himalaya) inferred from trace element constrained monazite and zircon chronology. Contributions to Mineralogy and Petrology 165, 349–372. https://doi.org/10.1007/s00410-012-0812-y.
- Ryan, P. D. & Dewey, J. F. (2019). The sources of metamorphic heat during collisional orogeny: the Barrovian enigma. Canadian Journal of Earth Sciences 56, 1309-1317. https://doi.org/10.1139/ cjes-2018-0182.
- Schneider, C. A., Rasband, W. S. & Eliceiri, K. W. (2012). NIH image to ImageJ: 25 years of image analysis. Nature Methods 9(7), 671-675. https://doi.org/10.1038/nmeth.2089.
- Scott, J. M., Palin, J. M., Cooper, A. F., Fagereng, A. & King, R. P. (2009). Polymetmorphism, zircon growth and retention of early assemblages through the dynamic evolution of a continental arc in Fiordland, New Zealand. Journal of Metamorphic Geology 27, 281-294. https://doi.org/10.1111/j.1525-1314.2009.00817.x.
- Selverstone, J. (1985). Petrologic constraints on imbrication, metamorphism, and uplift in the SW Tauern window, eastern Alps. Tectonics 4, 687–704. https://doi.org/10.1029/TC004i007
- Selverstone, J. (1993). Micro-to macroscale interactions between deformational and metamorphic processes, Tauern Window, Eastern Alps. Schweizerische Mineralogische und Petrographische Mitteilungen 73, 229–239.
- Selverstone, J., Spear, F. S., Franz, G. & Morteani, G. (1984). High-pressure metamorphism in the SW Tauern window, Austria: P-T paths from hornblende-kyanite-staurolite schists. Journal of Petrology 25, 501-531. https://doi.org/10.1093/ petrology/25.2.501.
- Skrzypek, E., Kato, T., Kawakami, T., Sakata, S., Hattori, K., Hirata, T. & Ikeda, T. (2018). Monazite behaviour and time-scale of metamorphic processes along a low-pressure/high-temperature field gradient (Ryoke Belt, SW Japan). Journal of Petrology 59, 1109-1144. https://doi.org/10.1093/petrology/egy056.
- Smye, A. J., Bickle, M. J., Holland, T. J. B., Parrish, R. R. & Condon, D. J. (2011). Rapid formation and exhumation of the youngest Alpine eclogites: a thermal conundrum to Barrovian metamorphism. Earth and Planetary Science Letters 306, 193-204. https://doi.org/10.1016/j.epsl.2011.03.037.
- Spear, F. (2010). Monazite-allanite phase S. relations in metapelites. Chemical Geology 279, 55-62. https://doi.org/10.1016/j.chemgeo.2010.10.004.
- Spear, F. S. & Pyle, J. M. (2002) Apatite, monazite, and xenotime in metamorphic rocks. In: Kohn M. J., Rakovan J. & Hughes J. M. (eds) Phosphates: Geochemical, Geobiological, and Materials ImportancePhosphates: Geochemical,

- Geobiological and Materials Importance, Vol. 48, pp. 293-336, https://doi.org/10.1515/9781501509636-010.
- Spear, F. S. & Wolfe, O. M. (2020). Revaluation of "equilibrium" P-T paths from zoned garnet in light of quartz inclusion in garnet (QuiG) barometry. Lithos 372-373, 105650. https://doi.org/10.1016/j.lithos.2020.105650.
- Spear, F. S., Thomas, J. B. & Hallett, B. W. (2014). Overstepping the garnet isograd: a comparison of QuiG and thermodynamic modeling. Contributions to Mineralogy and Petrology 168, 1059. https://doi.org/10.1007/s00410-014-1059-6.
- Stacey, J. S. & Kramers, J. D. (1975). Approximation of terrestrial lead isotope evolution by a two-stage model. Earth and Planetary Science Letters 26, 207-221. https://doi.org/10.1016/0012-821X(75 )90088-6.
- Steffen, K. J. & Selverstone, J. (2006). Retrieval of P-T information from shear zones: thermobarometric consequences of changes in plagioclase deformation mechanisms. Contributions to Mineralogy and Petrology 151, 600-614. https://doi.org/10.1007/ s00410-006-0073-8.
- Štípská, P., Hacker, B. R., Racek, M., Holder, R., Kylander-Clark, A. R., Schulmann, K. & Hasalová, P. (2015). Monazite dating of prograde and retrograde P-T-d paths in the Barrovian terrane of the Thaya window, Bohemian massif. Journal of Petrology 56, 1007-1035. https://doi.org/10.1093/petrology/egv026.
- Sun, S. & McDonough, W. F. (1989). Chemical and isotopic systematic of oceanic basalts: implication for mantle composition and processes. Geological Society, London, Special Publications 42, 313–345. https://doi.org/10.1144/GSL.SP.1989.042.01.19.
- Tholt, A., Mulcahy, S. R., McClelland, W. C., Roeske, S. M., Meira, V. T., Webber, P., Houlihan, E., Coble, M. A. & Vervoort, J. D. (2021). Metamorphism of the Sierra de Maz and implications for the tectonic evolution of the MARA terrane. Geosphere 17, 1786-1806. https://doi.org/10.1130/GES02268.1.
- Thomas, J. B. & Spear, F. S. (2018). Experimental study of quartz inclusions in garnet at pressures up to 3.0 GPa: evaluating validity of the quartz-in-garnet inclusion elastic thermobarometer. Contributions to Mineralogy and Petrology 173, 42. https://doi.org/10.1007/s00410-018-1469-y.
- Trettin, H. P. (1987). Pearya: a composite terrane with Caledonian affinities in northern Ellesmere Island. Canadian Journal of Earth Sciences 24, 224-245. https://doi.org/10.1139/e87-025.
- Trettin, H. P. (1998). Pre-carboniferous geology of the northern part of the Arctic Islands. Northern Heiberg Fold Belt, Clements Markham Fold Belt and Pearya. Geological Survey of Canada Bulletin
- Trettin, H. P. & Frisch, T. O. (1996) Map 1881A, Geology, Yelverton Inlet, District of Franklin, Northwest Territories scale 1:250,000. Ottawa: Geological Survey of Canada.
- Trettin, H. P., Parrish, R. R. & Loveridge, W. D. (1987). U-Pb age determinations on Proterozoic to Devonian rocks from northern Ellesmere Island, Arctic Canada. Canadian Journal of Earth Sciences 24, 246-256. https://doi.org/10.1139/e87-026.
- Trettin, H. P., Parrish, R. R. & Roddick, J. C. (1992) New U-Pb and <sup>40</sup>Ar-<sup>39</sup>Ar age determinations from the northern Ellesmere and Axel Heiberg islands, Northwest Territories and their tectonic significance. In: Radiogenic age and isotopic studies: Report 6. In: Geological Survey of Canada, Paper, Vol. 92-2, pp.3-30.
- Tsujimori, T. & Liou, J. G. (2004). Metamorphic evolution of kyanite-

- staurolite-bearing epidote-amphibolite from the Early Palaeozoic Oeyama belt, SW Japan. Journal of Metamorphic Geology 22, 301-313. https://doi.org/10.1111/j.1525-1314.2004.00515.x.
- Van der Molen, I. & Van Roermund, H. L. M. (1986). The pressure path of solid inclusions in minerals: the retention of coesite inclusions during uplift. Lithos 19, 317-324. https://doi. org/10.1016/0024-4937(86)90030-7.
- Viete, D. R. & Lister, G. S. (2017). On the significance of shortduration regional metamorphism. Journal of the Geological Society 174,377-392. https://doi.org/10.1144/jgs2016-060.
- Wang, J., Mao, Z., Jiang, F. & Duffy, T. S. (2015). Elasticity of singlecrystal quartz to 10 GPa. Physics and Chemistry of Minerals 42, 203-212. https://doi.org/10.1007/s00269-014-0711-z.
- White, R. W., Powell, R., Holland, T. J. B. & Worley, B. A. (2000). The effect of TiO2 and Fe2O3 on metapelitic assemblages at greenschist and amphibolite facies conditions: mineral equilibria calculations in the system K<sub>2</sub>O-FeO-MgO-Al<sub>2</sub>O<sub>3</sub>-SiO<sub>2</sub>-H<sub>2</sub>O-TiO<sub>2</sub>-Fe<sub>2</sub>O<sub>3</sub>. Journal of Metamorphic Geology 18, 497-511. https://doi. org/10.1046/j.1525-1314.2000.00269.x.
- White, R. W., Powell, R. & Holland, T. J. B. (2007). Progress relating to calculation of partial melting equilibria for metapelites. Journal of Metamorphic Geology 25(5), 511-527. https://doi.org/10.1111/j.1525-1314.2007.00711.x.
- White, R. W., Powell, R., Holland, T. J. B., Johnson, T. E. & Green, E. C. R. (2014). New mineral activity-composition relations for thermodynamic calculations in metapelitic systems. Journal of Metamorphic Geology 32, 261-286. https://doi.org/10.1111/jmg.12071.
- Whitney, D. L. & Evans, B. W. (2010). Abbreviations for names of rock-forming minerals. American Mineralogist 95, 185-187. https://doi.org/10.2138/am.2010.3371.
- Williams, I. S. (1998). U-Th-Pb geochronology by ion microprobe. In: McKibben, M. A., Shanks III, W. C., Ridley, W. I. (eds.) Applications of Microanalytical Techniques to Understanding Mineralizing Processes. Reviews in Economic Geology 7, 1-35.
- Williams, M. L. & Jercinovic, M. J. (2012). Tectonic interpretation of metamorphic tectonites: integrating compositional mapping, microstructural analysis and in situ monazite dating. Journal of Metamorphic Geology 30, 739-752. https://doi.org/10.1111/ j.1525-1314.2012.00995.x.
- Wolfe, O. M. & Spear, F. S. (2018). Determining the amount of overstepping required to nucleate garnet during Barrovian regional metamorphism, Connecticut Valley Synclinorium. Journal of Metamorphic Geology 36, 79-94. https://doi.org/10.1111/ jmg.12284.
- Wolfe, O. M. & Spear, F. S. (2020). Regional quartz inclusion barometry and comparison with conventional thermobarometry and intersecting isopleths from the Connecticut Valley trough, Vermont and Massachusetts, USA. Journal of Petrology 61, egaa076. https://doi.org/10.1093/petrology/egaa076.
- Wolfe, O. M., Spear, F. S. & Harrison, T. M. (2021). Pronounced and rapid exhumation of the Connecticut Valley trough revealed through quartz in garnet Raman barometry and diffusion modelling of garnet dissolution-reprecipitation reactions. Journal of Metamorphic Geology 39, 1045-1069. https://doi.org/10.1111/jmg.12601.
- Yang, P. & Pattison, D. (2006). Genesis of monazite and Y zoning in garnet from the Black Hills, South Dakota. Lithos 88, 233-253. https://doi.org/10.1016/j.lithos.2005.08.012.